ACOUSTIC RANGING IN A DYNAMIC, MULTIPATH ENVIRONMENT

BY

Michelle J. Weirathmueller

B.S. Geomatics Engineering, University of New Brunswick (2005)

THESIS

Submitted to the University of New Hampshire
in partial fulfillment of
the requirements for the degree of

Master of Science

in

Ocean Engineering

December 2008

This thesis has been examined and approved.

_____

Thesis Director, Thomas C. Weber,

Research Assistant Professor of Ocean Engineering, UNH

_____

Larry Mayer,

Professor of Ocean Engineering and Earth Sciences, UNH

_____

Lloyd Huff,

Research Professor of Ocean Engineering, UNH

_____

David Wells,

Affiliate Professor at The Center for Coastal and Ocean Mapping, UNH

_____

Date

DEDICATION

I would like to dedicate this work to my father, who has given me sage advice during the toughest times, and to my mother who has always been there to put things in perspective. This work is also dedicated to Stephanie, Andrea, and Jakob, who have been forced, against their will, to learn about underwater acoustic measurements.

I would also like to especially thank Val Schmidt for his endless support, advice, and friendship.

Most of all, I owe a debt of gratitude to my husband, John, who has continually cheered me on, made me laugh, and kept me sane.

ACKNOWLEDGEMENTS

I would like to acknowledge and thank my thesis advisor, Tom Weber, who has given up countless hours of his time teaching me about everything from acoustics theory to soldering. I would also like to acknowledge the assistance and support provided by my committee: Larry Mayer, Lloyd Huff, and Dave Wells. Val Schmidt has spent hours with me scribbling math on the white board, and having extended discussions on the details of this project; he has steered me away from dangerous conclusions innumerable times. Several of the graduate students at CCOM have helped me with revisions and practice presentations along the way, including Janice Felzenberg, Mashkoor Malik, Gretchen Imahori, Nick Forfinski, Lynn Morgan, Luis Rosa, Monica Wolfson, Brian O'Donnell, and Rochelle Wigley. Other faculty members have given generously of their time including Jim Irish, Shachak Pe'eri, and Kurt Schwehr.

The field work and experiment preparations would have been impossible without the tireless assistance provided by Ben Smith, Glenn McGillicuddy, Andy McLeod, Paul Lavoie, and John Wray. Will Fessenden, Lester Peabody, and the rest of the IT team helped things to run smoothly, and their hard work is much appreciated.

TABLE OF CONTENTS

LIST OF TABLES

LIST OF FIGURES

ABSTRACT

ACOUSTIC RANGING IN A DYNAMIC, MULTIPATH ENVIRONMENT

by

Michelle J. Weirathmueller
University of New Hampshire, December, 2008

An acoustic experiment was carried out in October 2007 in Portsmouth Harbor, New Hampshire, to measure the effects of environmental variability on acoustic range measurements over a distance of 948 meters. A fixed source and receiver measured the one-way travel time and signal level fluctuations over four days. Observations of wind, sound speed, and tide, as well as current speed predictions were used to assess their effects on the acoustic measurements. The environmental data collected during this experiment showed variability at many scales, both temporally and spatially throughout the harbor. The acoustic data revealed the presence of multipath arrivals, with 2-3 strong arrivals for each transmitted ping. A simple geometric model was used, along with ray-tracing, to describe fluctuations in arrival time and signal level. Acoustic travel times between a fixed source and receiver were converted to range measurements and compared with GPS-derived ranges. This study provides a basis for understanding the capabilities and limitations of acoustic travel time measurements in Portsmouth Harbor, or similar dynamic multipath environments. Results showed an overall spread in range of between five and eight meters over the total range of 948 meters, with greater precision and accuracy possible with additional processing.

CHAPTER 1

INTRODUCTION

Portsmouth Harbor, New Hampshire is a shallow, dynamic estuary. There are five main rivers that flow into the Piscataqua River basin, which in turn drain into Portsmouth Harbor: Lamprey River, Oyster River, Cocheco River, Winnicut River, and Exeter River. There is a significant amount of seasonal variation in freshwater inputs due to snow-melt and precipitation. Freshwater inputs are mixed with saline ocean water by strong semi-diurnal tides. The tidal range is approximately 3 meters, and tidal currents reach speeds exceeding 60 cm/s. The area of interest in this project is the lower part of the harbor: about 1.5 km^2 between the Fort Point Lighthouse on Newcastle Island and the mouth of the harbor (Figure 1-1). The average depth in the area is thirteen meters, with a deeper channel on the eastern side.

Portsmouth Harbor has been the focus of numerous hydrographic and seafloor characterization studies including single beam, multibeam, sidescan and LIDAR surveys (e.g.,[2], [3], [4]). Ground-truthing of seafloor type has been accomplished in many areas using still cameras, video cameras, and also by collection of physical samples for laboratory analysis ([1], [5]). In addition to vessel-based studies, there is growing interest in the use of remotely operated vehicles (ROVs) and autonomous underwater vehicles (AUVs) for seafloor mapping. AUVs are of particular interest as they can provide a data collection platform that can be operated very close to the bottom and therefore would not interfere with vessel traffic in the busy channel. In heterogeneous environments, like Portsmouth Harbor, high positioning accuracy (less than 1 m) for these underwater sensors and vehicles is required in order to match the positioning accuracy of, for example, a vessel-mounted multibeam sonar.

Figure 1-1: The Portsmouth Harbor experiment location (shown by the red box).

Positioning methodology for underwater vehicles typically involves an integration of the vehicle's speed over time, combined with a heading measurement to provide position [6]. Speed may be measured using a speed-through-water sensor. The problem with this type of measurement is that the speed of the vehicle is difficult to separate from the current speed. If operations are close enough to the seafloor, a Doppler velocity log (DVL) can be used to measure the speed over ground [7]. Both of these systems suffer from significant drift over time as the velocity is integrated to estimate position. Inertial navigation systems

(INS) combine measurements of acceleration and direction and use a double integration to determine position [8]. These are frequently used in conjunction with DVLs. Inertial navigation systems are self contained and do not require communications with an external source, however, they are often cost prohibitive and are problematic for battery-operated systems due to high power consumption. INS and Doppler systems still suffer from drift and require regular position fixes to maintain good positional accuracy. These position fixes may be obtained by bringing the vehicle to the surface so that a GPS fix can be established. Alternatively, the position fixes can be provided by an underwater acoustic positioning system.

Some of the more common acoustic positioning techniques include ultra-short baseline (USBL), short baseline (SBL), and long baseline (LBL) positioning ([9], [10], [11]). A USBL positioning system utilizes a transducer that tracks moving transponders in the water column. The transducer is made up of several closely spaced elements that measure phase differences to estimate bearings and elevation angles. Bearing and elevation angle are combined with travel time measurements between the transducer and the transponders to estimate range for USBL positioning. The SBL method is based on a similar concept, but the hydrophones are more widely spaced (5 - 20 m) and instead of phase differencing, arrival time difference is used to measure bearing and elevation angle [9]. Both USBL and SBL systems are commonly mounted on vessel hulls, but can also be bottom-moored [12] or mounted on surface buoys [13]. Rather than measuring azimuth and elevation angle from a closely spaced array of transducer elements, LBL systems measure ranges between a widely spaced array of transponders and a moving pinger.

Converting a travel time measurement to a range requires knowledge of the sound speed along the entire propagation path. The travel time measurement becomes complicated when the signal interacts with one or more boundaries before reaching the receiver. For this reason, time-of-arrival measurements have typically been utilized in deep water environments where the pinger and receivers are assumed to be contained within a single sound speed layer ([14], [9], [11]). Once a range estimate is obtained, a least squares algorithm can

3

then be used to estimate the position of the pinger utilizing either a hyperbolic or spherical solution ([15], [16])

These acoustic positioning systems can be reduced to two fundamental measurement types: time-of-arrival detection and phase differencing. The long range time-of-arrival measurements that would be used in an LBL-type solution are the focus of this thesis, in which the viability of such an approach in a shallow water environment such as Portsmouth Harbor will be explored.

The combination of strong currents, the shallowness of the channel, and complicated sound speed caused by mixing between fresh and ocean waters, poses challenges for acoustic range measurements in a shallow water environment such as Portsmouth Harbor. In a shallow channel such as Portsmouth Harbor, multipath structure is expected with several arrival paths potentially reaching the receiver very close together in time. This multipath structure might pose difficulties in the isolation and detection of a direct path arrival. Several studies have examined the specific shape of the multipath arrivals in a shallow acoustic channel to derive various boundary properties and environmental parameters. Smith [17] investigated the average impulse response in a shallow channel having a small (less than 3m/s) change in sound speed. Experimental data was gathered in 190 meters of water over 5-50 km and was compared with theoretical predictions. The amplitude and phase of the received signal proved to be dependent on the range from the source and the properties of the seabed and water surface. Aubauer et al. [18] used the temporal spacing of multipath arrivals in shallow water to estimate the location of a phonating dolphin. Deffenbaugh et al. [19] developed a technique that uses multipath arrivals to invert for spatial and temporal sound speed structure to improve positioning accuracy in complex environments . Deffenbaugh's technique combines multipath arrival spacing with ray tracing to iteratively obtain a position estimate, even when some of the multipath arrivals fade. Deffenbaugh's model deals specifically with the fading multipaths due to bathymetric obstructions, such as a shallow area between the source and reciever. Utilizing a system such as that introduces increased complexity in the implementation of a positioning system; however, in some

conditions it might be a necessary step.

In addition to the complexities arising from multipath arrivals, inhomogeneities in sound speed along the acoustic path will cause refraction and scattering, leading to sample-to-sample variations in the received signal [20]. Several studies have looked at the fluctuations in the received signal that are due to turbulence. Di Iorio and Farmer [21] make estimates of current, temperature, and salinity structure based on the fluctuations resulting from turbulence. Meredith et al. [22] look at direct path arrivals in shallow turbulent water where both swell and turbulence have an effect on the received signals. They found that the amplitude fluctuations seen in the direct path signal were predominantly due to turbulence in the water column.

Other studies have investigated the amplitude variability and frequency modulation caused by interactions with a rough sea surface. Mackenzie [23] describes an experiment in which a transmitted CW pulse experiences frequency modulation as well as amplitude fluctuations of up to 50 dB, arising from interactions with a rough sea surface. Dahl ([24]) studied the scattering of signals due to surface roughness and bubbles just below the surface. In this study, Dahl compared field measurements using bistatic surface scattering models. Plots of measured data show a minor drop in amplitude between the direct path signal and the surface bounce signal (less than 5 dB), however, the bottom bounce was shown to have resulted in a significant decrease in amplitude of between 20 - 25 dB. Surface grazing angles for these two examples were 13°-14°. Bottom grazing angles for the first bottom bounce arrival were between 14°-25°.

McDaniel [25] reviewed research on sea surface reverberation. Her paper described the reverberation levels that have been observed in high frequency transmissions in shallow water. These were largely attributed to subsurface bubbles, and scattering from a rough sea surface. Increased reverberation levels have been observed in nearshore waters, as compared with the open ocean, due to increased production of subsurface bubbles.

Amplitude fluctuations might also arise from signals interacting with the bottom. The bottom is relatively static at short time scales; however, individual transmitted signals might

interact with the bottom at slightly different locations, giving rise to different scattering effects. Choi and Dahl [26] looked at bottom loss at several frequencies and incidence angles, and showed ping-to-ping variability of single-bottom-bounce received signals on the order of 5-10 dB. Rouseff and Ewart [27] describe several simulations of shallow water (24-68 m depth over 10 km range) environments, with changing sea surface and bottom parameters. They show the potential for large variability from these combined effects, even without consideration of complexities in the water column.

The combined outcome of these cited studies indicates that measuring acoustical ranges in Portsmouth Harbor will be complicated by turbulence in the water column, interactions with the bottom, and interactions with the rough sea surface and sub-surface bubbles. To empirically evaluate the effect of these variables and to see how they affect the accuracy of acosutic positioning, a one-way acoustic propagation experiment was carried out in Portsmouth Harbor during October 2007. A fixed source and receiver were separated by 948 meters. The average depth between the source and receiver was thirteen meters. Wind, modeled current speed, sound speed and tidal data were collected in order to assess their effects on the acoustic measurements.

CHAPTER 2

EXPERIMENT DESCRIPTION

The research described here was conducted in the lower part of Portsmouth Harbor, New Hampshire, south of the bend in the channel at Newcastle Island (Figure 2-1). At this site, a one-way acoustic propagation experiment took place over four days in October 2007. A fixed, bottom-mounted source on the west side of the channel transmitted once per second, and the signals were received at a hydrophone mounted on Fort Foster pier (source and receiver locations are shown in Figure 2-1). Simultaneous environmental measurements were collected, including sound speed profiles, tide height, and wind speed, as well as modeled current speed. This experiment emulates the type of measurement that would be made when tracking an AUV across the harbor. A sketch of the experimental setup (Figure 2-2), shows the position of the bottom-mounted pinger and the hydrophone mounted on the pier piling.

Multibeam echosounder data was collected in November 2000 by the NOAA Ship Whiting using a Reson 8101 (Figure 2-1). The multibeam image indicates a depth range of between 3 - 24 meters, with a maximum depth of 20 meters along the transect between the source and receiver. The multibeam bathymetric data shows a sand wave field in the middle of the channel, south of Fort Point. The channel deepens to the east of the sand wave field. A few rocky outcrops can be seen on the eastern side of the deeper channel. The bathymetric profile along the transect between the acoustic source and receiver is shown in Figure 2-3. This profile reveals that the bathymetric data does not cover the entire extent of the acoustic path; it ends approximately 170 m short of the hydrophone location. Starting from the west, the profile shows a gradual increase in depth, with the deepest point (20 meters depth) at a horizontal range of 485 meters from the source, which is very close to
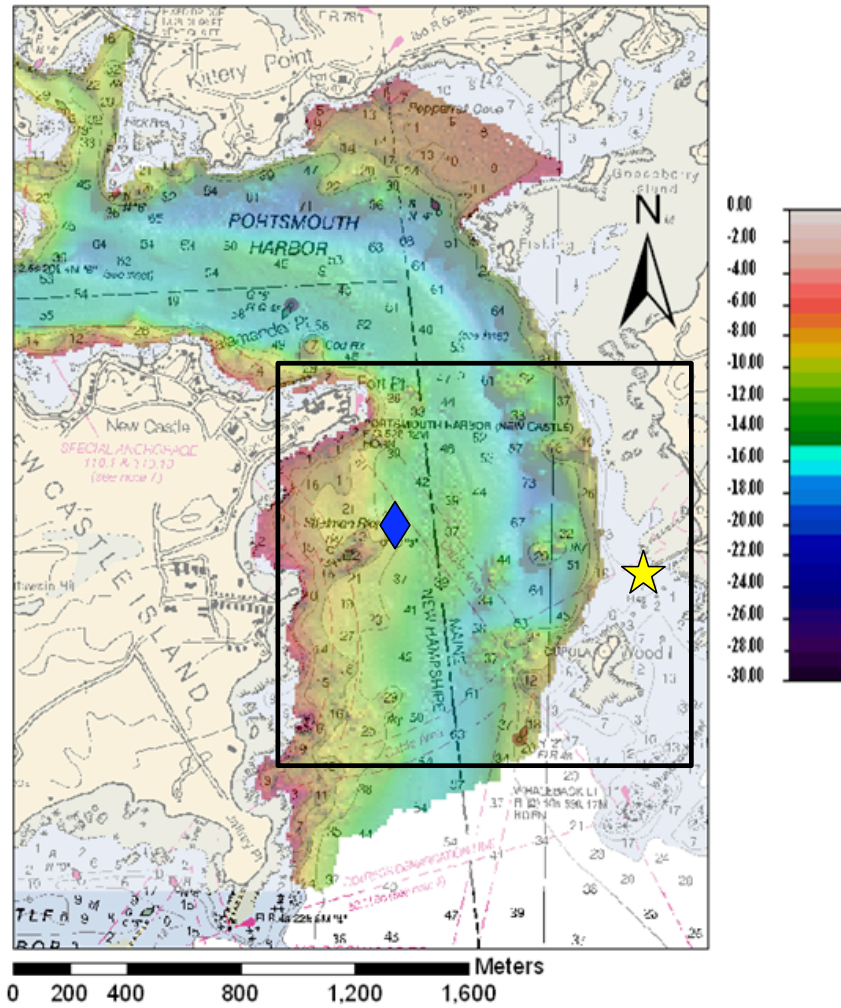
Figure 2-1: Multibeam bathymetry is overlaid on the chart (NOAA Chart number 13283-1). The hydrophone is shown as a star, and the diamond shaped marker denotes the approximate source location. The average depth across the channel is thirteen meters, and the range between the source and receiver is 948 meters.

the halfway point between the source and the receiver.

Ward [1] describes the results of sedimentological surveys conducted in the Piscataqua River estuary. These results show that in the area of this experiment, the surficial sediment consists mainly of sand, gravel, and some areas of exposed bedrock (Figure 2-4). Along the
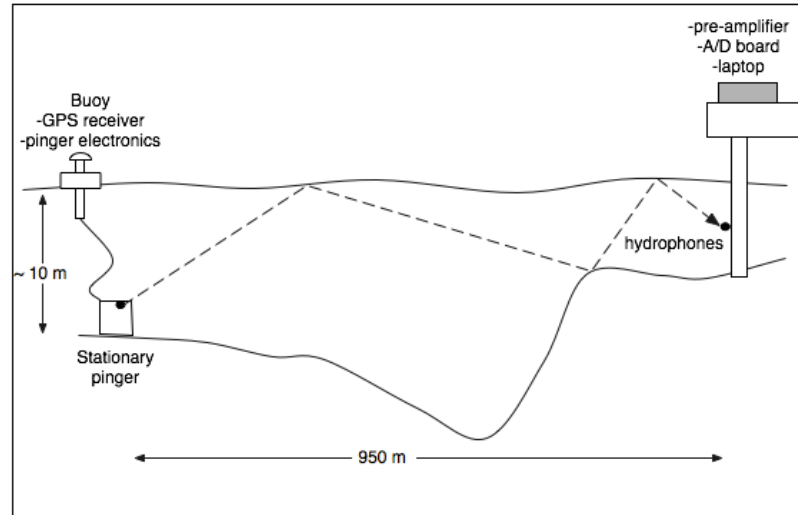
Figure 2-2: A sketch of the pinger and hydrophone setup used in the experiments. The average depth of water was 13 meters, with a maximum depth along the profile of 20 meters at the center of the channel.

transect between the fixed source and receiver, the surficial sediment is mostly gravel, with large regions of sand near the source (the sand wave field), and also on the eastern side of the channel.
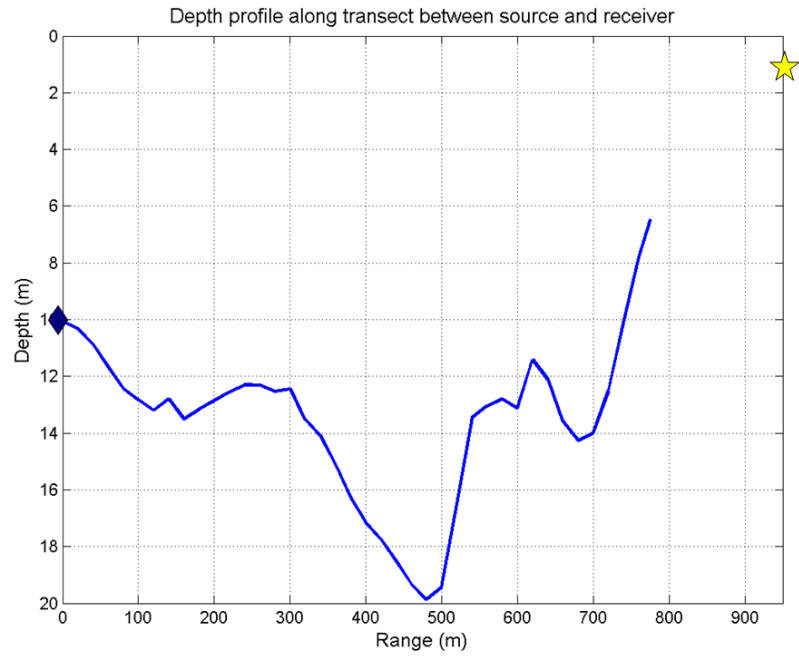
Figure 2-3: The bathymetry along the transect between the acoustic source and receiver was extracted from the multibeam data. There is a gap of approximately 170 meters between the multibeam data and the receiver at Fort Foster pier. The acoustic source is denoted by the blue diamond, and the receiver is denoted by the yellow star (the same source and receiver positions shown in Figure 2-1.
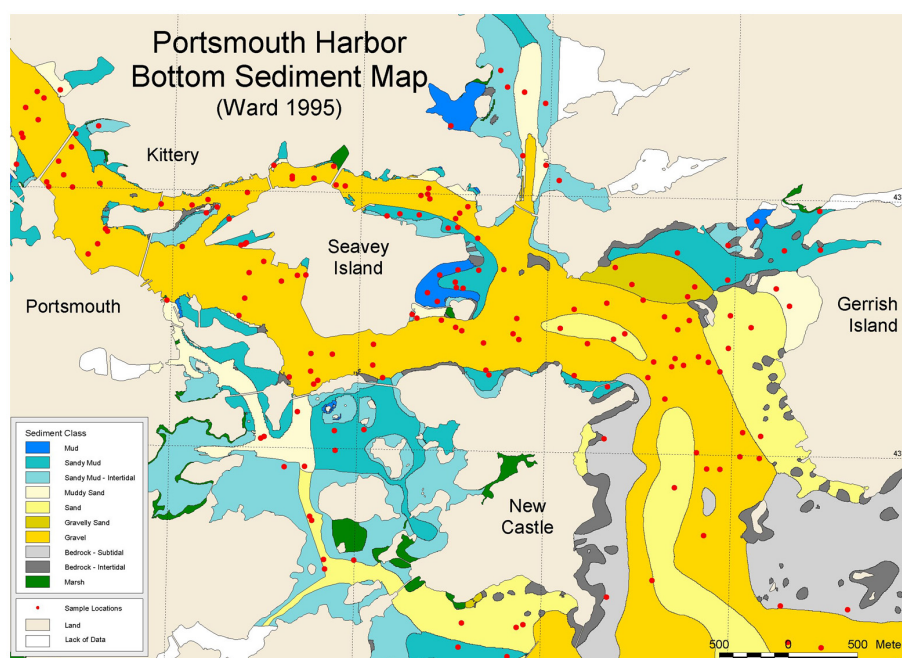
Figure 2-4: Portsmouth Harbor sediment map - from Ward [1].

2.1 Acoustic Measurements

The acoustic measurements were made using a Reson TC-4013 hydrophone. Acoustic data were collected from 23-26 October 2007, for several hours each day. The hydrophone was located at approximately 2 meters above the sea floor and at high tide it was submerged to a depth of approximately 3.5 meters. The received acoustic data was passed through a Stanford Research Systems (SRS) pre-amplifier, which was used to filter and amplify the signal. The SRS pre-amplifier had its high pass filter set to 10 kHz and its low pass filter set to 100 kHz. Voltages representative of acoustic pressures were digitized using a National Instruments data acquisition device sampling at a rate of 100 kHz. The data acquisition device was interfaced with a laptop on Fort Foster pier. The laptop used MATLAB software to configure the data acquisition device and log the data. Both the transmitter and receiver systems received inputs from GPS receivers providing a one pulse-per-second (PPS) signal that was used to synchronize the acoustic signal transmit time at the pinger and the receive time at the hydrophone. Laboratory measurements collected prior to the experiment showed differences between PPS signals from the two GPS receivers to be less than 200 nanoseconds.

The hydrophone was positioned using a Trimble Zephyr geodetic GPS antenna fixed to the top of the pier piling where the hydrophone was installed. Data was collected for over two hours to allow use of the National Geodetic Survey's On-line Positioning User Service (OPUS). This service provides processing of GPS data using corrections from three nearby CORS stations [28]. The positional uncertainty provided by OPUS was 0.108 m in the Northing direction, and 0.053 m in the Easting direction. The most significant error that might be introduced into the GPS position estimate is the horizontal position of the GPS antenna in relation to the hydrophones lower on the pier piling. This bias error is estimated to be 0.25 m.

The bottom-mounted source was a SensorTech SX-30 free-flooded ring transducer. The source had an omni-directional beam pattern in the plane perpendicular to the axis of the ring (horizontal), and a 60° toroidal beam pattern in the axial dimension (at 30 kHz).

The source had a resonant frequency of 30 kHz (usable frequency range between 20 and 40 kHz). It was mounted 25 centimeters from the bottom on a weighted frame and was linked via cable to a buoy at the surface containing the pinger electronics and the GPS receiver that provided the 1 PPS signal for time synchronization. This pinger enabled observation of acoustic signals over time from one fixed location in order to isolate signal fluctuations caused by the environment. The time series recorded at the hydrophone during the experiment was filtered using a 7th order Butterworth filter with a bandwidth of 10 kHz (35-45 kHz). The received time series and the recoreded transmit signal were quadrature demodulated before performing the matched filtering operation.

To estimate the position of the pinger, several range measurements were made to a hydrophone on the ram of the R/V Coastal Surveyor. The Coastal Surveyor maneuvered around the pinger, within a horizontal range of between 50-100 m, collecting acoustic ranges between the bottom-moored source, and the hydrophone on the ram of the vessel. This range intersection approach was modeled after a range intersection technique used in land surveying, which is described in Anderson and Mikhail [29]. The transmit and receive times were synchronized using the 1 PPS signal from the GPS. The hydrophone on the Coastal Surveyor was positioned using real-time kinematic GPS (RTK GPS) [30]. Vessel attitude and motion were measured using a POS/MV inertial motion unit and was used to translate the GPS position from the GPS antenna to the hydrophone. Each range measurement from a known vessel position defines the surface of a sphere, using the assumption that the travel paths follow straight lines between the pinger and hydrophone. The point where the spheres intersect is the location of the unknown target. To solve for the unknown source position in three dimensions requires four range measurements from known positions. Each time the pinger was positioned, several hundred range measurements were collected over a span of five to ten minutes. This provided redundancy, allowing for a least squares estimate to be calculated. The general case of least squares estimation was used, based on methodology outlined in Cooper ([31]) and Anderson and Mikhail ([29]). This method requires an initial estimate of the unknown coordinates, and iterates until the solution converges, given the

measured values, and their uncertainties. The pinger positioning methodology is described in more detail in Appendix A. The pinger position was determined four times: once on 23 October, twice on 24 October, and once on 25 October. The standard deviations in the northing and easting directions were all less than 15 centimeters (see Table A.1).

A piecewise chirp signal was transmitted from the pinger in order to increase the bandwidth, and hence increase the temporal resolution of time-of-arrival measurements. The chirp signal, transmitted at a 1 Hz repetition rate was a combination of seven 1.02 ms CW pulses in 1kHz steps from 37-42 kHz. The 'dead time' spacing between each of the seven CW pulses was 0.40 ms. The piecewise chirp signal shown in Figure 2-5 was received on the Reson TC-4013 hydrophone.
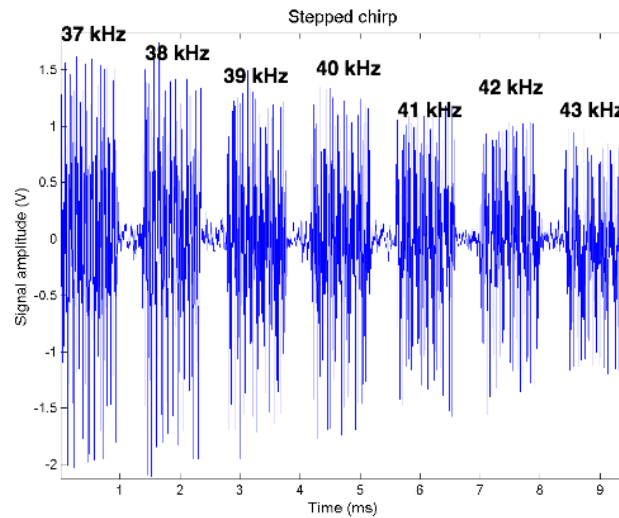
Figure 2-5: The signal shown here was measured in the tank prior to the October experiment, and was the same signal that was transmitted from the bottom mounted source during this experiment. The signal consists of seven one-millisecond segments from 37 kHz - 43 kHz.

Both the signal levels and the time-of-arrival measurements were extracted from the output of a matched filtering operation. This process was accomplished by cross-correlating

the known transmit signal $s(t)$ with the received signal $x(t)$ over the length of the signal T. (Equation 2.1). The reference signal used in the cross correlation was the transmit signal that was measured in the University of New Hampshire acoustic test tank prior to deployment in the harbor. The received signal contains a version of the transmitted pulse that has experienced attenuation α and is at an unknown time delay [32]. The location of the maximum peak of the cross-correlator output $y(T)$ when the signal is present gives the time delay:

$$y(T) = \int_0^T x(t)s(t)dt. \tag{2.1}$$

When the delay between the matched filter and the signal in the data is zero, the theoretical result is proportional to an autocorrelation of the transmit pulse. The shape of the autocorrelation is shown in Figure 2-6. The width of the main lobe, at 3 dB down from the maximum, is 0.128 ms, which gives an upper limit to the time resolution of the matched filtering algorithm. The effective duration of the pulse is 0.128 ms. The sidelobes in Figure 2-6 are important since they may appear in the acoustic data as artifacts. The drop in amplitude from the main lobe to the first sidelobes is 17.5 dB. The sidelobe spacing is 1.3 milliseconds between the main lobe and the first sidelobe.

2.2   Environmental Measurements

One of the most critical measurements in computing a travel distance based on travel time is the sound speed along the propagation path. Not only would the effects of refraction cause the travel path to bend and slightly change the path length, but since the water depth is small relative to typical horizontal distances, slight changes in the refraction index could change the number of interactions with the surface or bottom. The number of boundary interactions, or bounces, can affect both the time of arrival and the signal strength at the receivers. Three methods were used to estimate sound speed in the harbor: conductivity-temperature-depth (CTD) casts, sound velocimeter measurements at a fixed location, and a CTD chain [33].
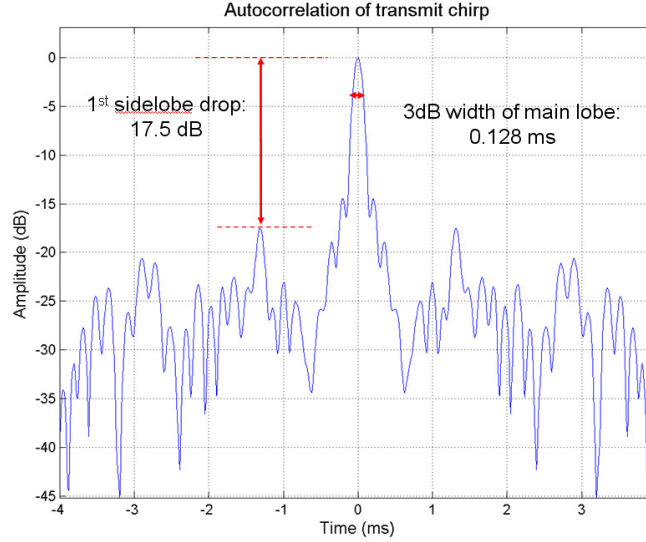
Figure 2-6: The autocorrelation of the transmit pulse.

Of the three methods, the CTD chain (figure 2-7) provided the most continuous sampling of the sound speed through the water column. The CTD chain, which was borrowed from The Pennsylvania State University, consisted of a series of CTD sensors that could be clamped onto a cable to allow for continous measurement at 1 Hz intervals. The CTD chain was deployed for several hours on the final day of the data collection. It measured a vertical profile of salinity and temperature through the water column from a vessel anchored in the middle of the channel. The CTD chain took a measurement once per second providing high resolution time series data for the entire water column using 18 sensors spaced at approximately 0.5 meter intervals. The sensors were deployed on a weighted cable. The temperature and salinity data were later converted to sound speed using the Del Grosso sound speed equation [34].

A Seabird CTD profiler (model: SBE 19plus V2) was used to determine sound speed as a function of depth several times each day for the first three days along the transect between the source and receiver, using the Del Grosso sound speed equation [34]. On the fourth day, when the vessel was moored and the CTD chain was taking measurements, Seabird CTD profiles were collected once every half hour at the same location to provide a check on the

16
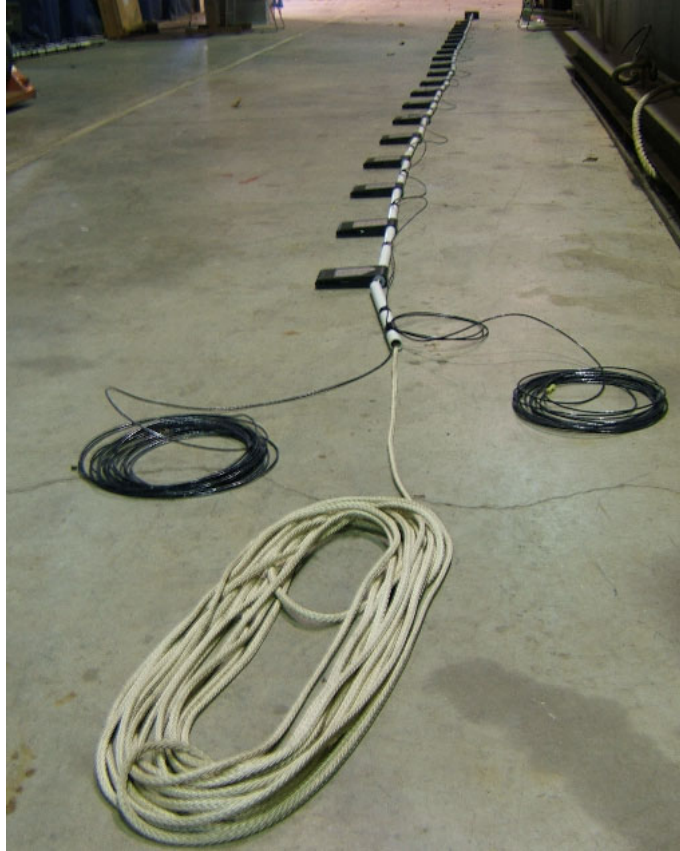
Figure 2-7: The CTD chain consisted of 18 sensors attached to a cable, spaced at approximately 0.5 m increments.

reliability of the CTD chain measurements.

An Odom Digibar Pro sound velocimeter was installed on the pier piling next to the hydrophone. It measured sound speed continuously by measuring the travel time over a known path length. The Digibar measured sound speed data continuously at the depth of the hydrophone.

In addition to changes in sound speed, the large tidal variation could also have an effect on the acoustic measurements. The tidal range of more than three meters was expected to affect the multipath structure, potentially changing the spacing between subsequent multipath arrivals, and also causing an increased spread in time of the matched filter output where the different arrivals overlap. The three-meter tidal range in the area is significant, considering the relatively shallow depths (maximum 20 meters depth along the transect

between the acoustic source and receiver). Tide heights were retrieved from the NOAA tide station located at Fort Point, 0.5 km up-river from the experiment location (Station ID 8423898).

Tidal currents were measured using an Acoustic Doppler Current Profiler (ADCP) as part of a NOAA experiment from May to July, 2007. Tidal current predictions for 23-26 October were generated using T_TIDE and T_PREDIC, tidal analysis software created for MATLAB [35]. T_TIDE was used to find the tidal current constituents of ADCP data collected from May to July 2007. The T_PREDIC software used these constituents to predict the current for the time of the experiment.

Wind data was gathered from the Isles of Shoals meteorological station, which is part of the Coastal-Marine Automated Network (C-MAN). The Isles of Shoals are located approximately 8 km offshore to the south-east of the experiment location. The wind measurements are reported at the height of the instrument, which was 32.3 meters above mean sea level.

CHAPTER 3

RESULTS

3.1   Environmental Observations

The spatial and temporal sound speed structure, as well as the magnitude of the sound speed changes in the harbor, are essential for understanding the acoustic measurements. The level of sound speed stratification in shallow water can affect the number of surface bounces and bottom bounces any given ray will experience. Increased sound speed stratification will result in stronger refraction, possibly changing the number of surface and bottom bounces. Having knowledge of the speed of sound along the acoustic path is also critical for converting travel time measurements to travel distance and ultimately to ranges. The combination of the Seabird CTD profiler, the CTD chain, and the Digibar sound velocimeter showed a complicated sound speed structure in the harbor, with rapid changes occuring over short time scales, and spatial variability across the harbor.

The Digibar sound velocimeter mounted on the pier piling near the hydrophone made continuous measurements throughout each day of acoustic data collection. The Digibar sound speed data is shown in Figure 3-1. These figures show changes of up to 5 m/s over the course of a day, and a spread of 8 m/s over all four days. To put this in the context of a range estimate, a sound speed change of 5 m/s over a range of 1 km would be approximately equivalent to a 3.4 m change in the range estimate. Long period fluctuations are visible with dominant time scales of several hours.

The Seabird CTD data collected on 24 October along the transect between the fixed source and receiver illustrates the spatial variability in sound speed in the harbor. Figure 3-2 shows an example of the CTD cast data measured across the transect between the fixed
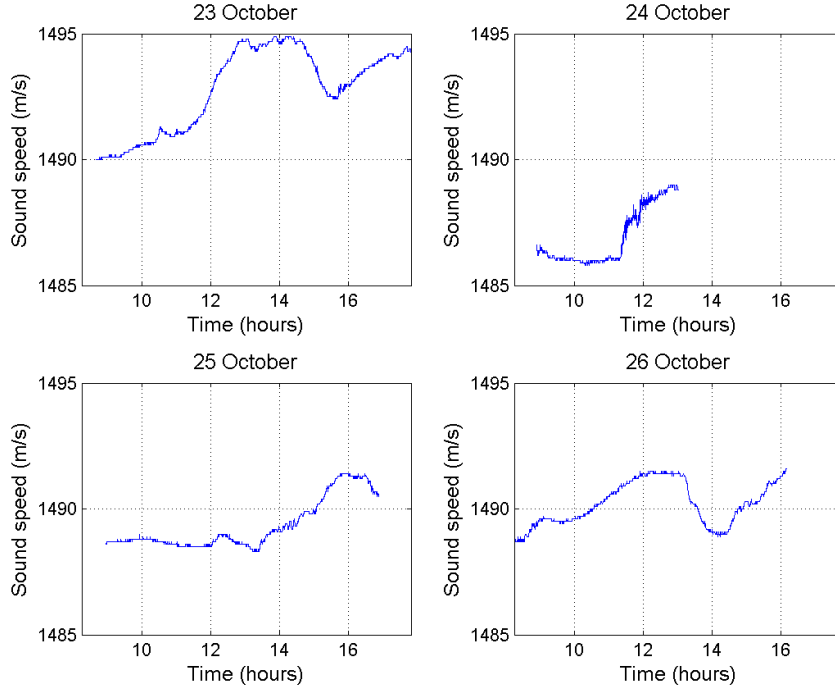
Figure 3-1: Digibar data during the four days of acoustic data collection.

source and receiver. The colors of the sound speed profiles on the right correspond to the CTD cast locations marked on the chart on the left. The casts were collected within a ten-minute span, and show the sound speed profiles on the western side of the harbor are uniform, while those on the eastern side, are stratified. Appendix B contains all of the CTD casts measured during the experiment.

On 23 October, only two Seabird CTD transects were completed, for a total of 13 casts. All of these casts were collected before 12:00, after which point the sea state prevented safe CTD deployment. These two transects revealed a large degree of vertical stratification (up to 4 m/s difference between surface and bottom), as well as a large degree of horizontal variability (up to 3 m/s difference in sound speed for a given depth at different locations). Most of the profiles on this day showed strong vertical stratification, with the exception of the profiles measured on the eastern side of the harbor in shallow water (less than 5 m depth).
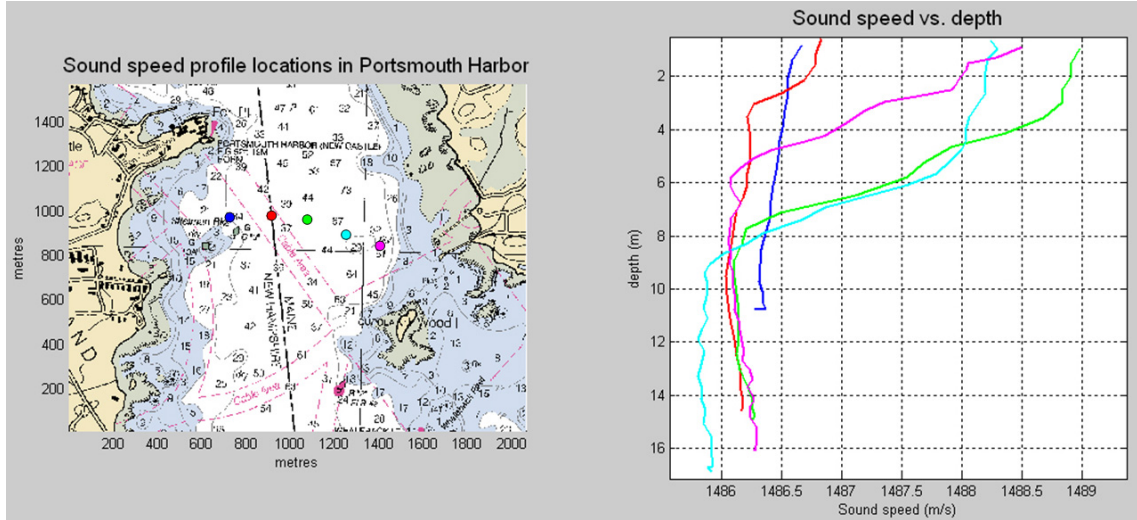
Figure 3-2: Seabird CTD cast locations are shown as colored dots on the chart on the left, and the corresponding sound speed profiles are on the right. The color of the profiles matches the color of the cast location. This transect was collected on 24 October starting at 12:56

The Seabird CTD casts collected on 24 October showed differences in the level of stratification between at different locations in the harbor. In the deeper part of the channel, the sound speed profiles appeared more stratified, with surface to bottom differences of up to 3 m/s. In the region of the sand wave field, and also in the shallow water near the receiver, the sound speed profiles were more uniform (Figure 3-2).

The Seabird CTD casts collected on 25 October were indicative of more vertical mixing than on any of the other days. Most measurements on this day did not vary by more than 1 m/s with depth or with spatial location, with the exception of shallow surface layers of higher sound speed. These profiles appear in the transects that take place at 12:52 and at 13:36.

The CTD chain data was collected on 26 October, and provides the most continuous monitoring of the sound speed depth profile in one location. The CTD chain data was collected for 5.5 hours. The Seabird CTD casts taken every half hour at the same location continued 1.5 hours past the end of the CTD chain data. Figure 3-3 shows the temperature

and salinity data collected using the CTD chain, along with the corresponding sound speed. The measured salinity remained between 31-33 (practical salinity scale), while the temperature varied between 9.5 and 11.5 degrees Celsius. From the start of the day until 11:30, the CTD chain data shows weak stratification. After 11:30, the stratification increases, with a higher sound speed layer appearing at the surface. An abrupt increase in mixing is observed after 14:00.
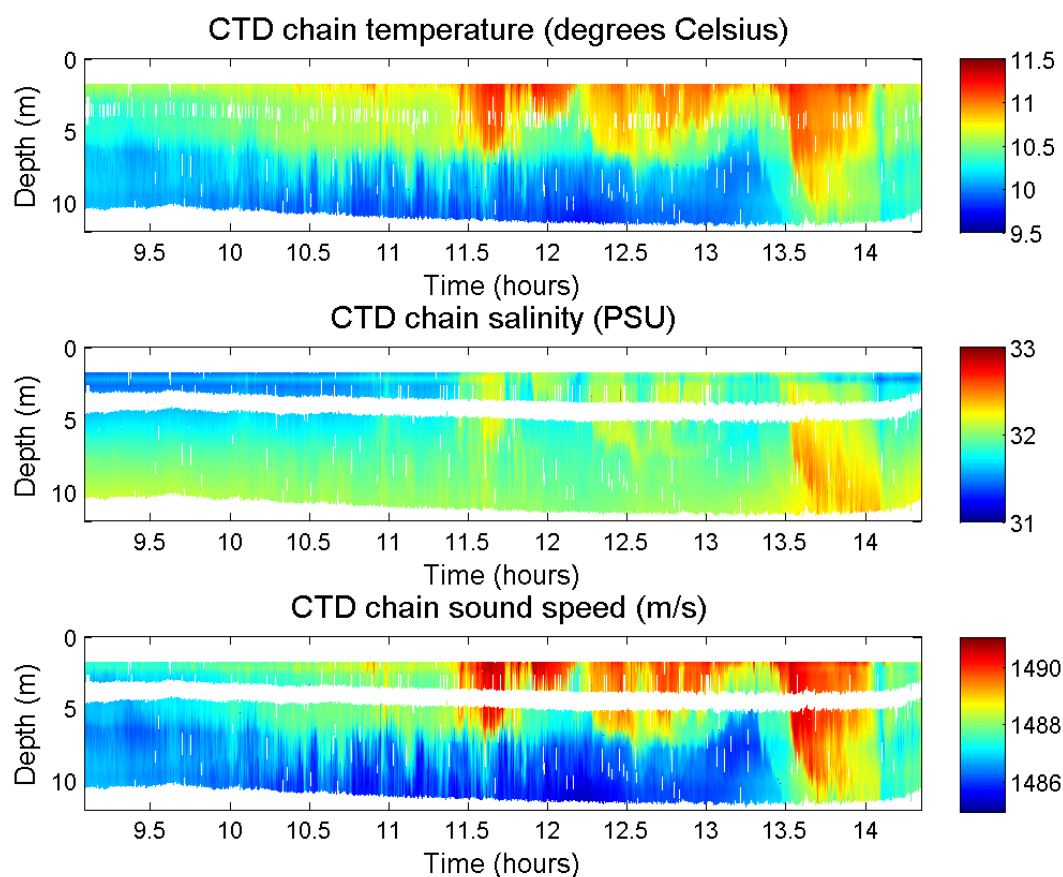
Figure 3-3: The three plots in this figure show the CTD chain data. The top plot shows temperature, the middle plot shows salinity, and the bottom plot shows sound speed.

The Digibar sound velocimeter data provides the most continuous measurement of sound

speed over the course of the experiment, and is the simplest choice for converting all of the acoustic time-of-arrival data to ranges. The Digibar data was compared with the Seabird CTD data to ascertain whether the sound speed at the Digibar location is representative of the sound speed over the entire acoustic travel path. Figure 3-4 shows a comparison of the Digibar sound velocimeter measurements with the CTD casts in two ways. The first is a comparison with the depth-averaged sound speed for each CTD cast, and the second is a comparison with the CTD measurement at the depth of the Digibar sensor (this depth was corrected for changes in tide height). This figure shows the Digibar measurements to be consistently higher than either the depth average or the Seabird CTD measurement at the Digibar depth. The mean difference over all of the measurements taken at the same depth is 1.6 m/s with a standard deviation of 1.4 m/s. A 1.6 m/s change in sound speed corresponds to difference of approximately 1 m in range for a nominal travel time of 0.64 ms.
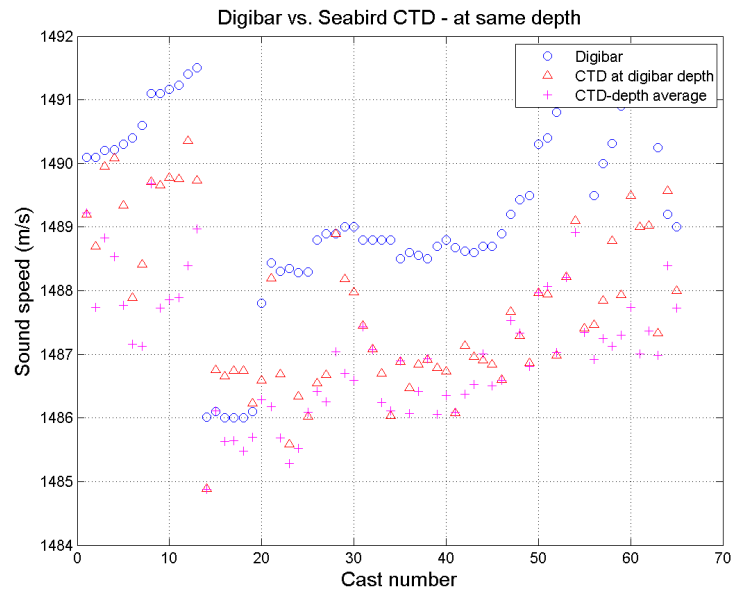
Figure 3-4: Digibar sound velocimeter measurement compared with the Seabird CTD depth averaged profiles, and the Seabird measurement at the depth of the Digibar.

The tidal range during the time of the data collection reached a maximum of 3.5 meters. The currents were predicted from measurements several months prior to the experiment, and therefore those shown here will not include any anomalous current events that might have occured during the experiments. Modeled currents and measured tides during the data collection times are shown in Figures 3-5 and 3-6. Positive current velocity values indicate flood, and negative values indicate ebb. Modeled ebb currents were typically faster than flood currents. The maximum modeled current speeds during this experiment reached 67 cm/s.
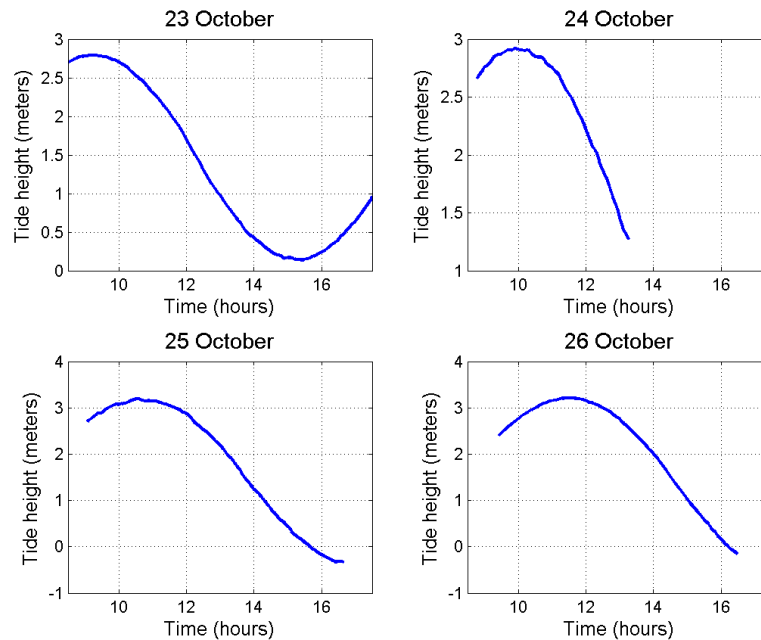
Figure 3-5: Tide measured at Fort Point at the time of the experiment.

The wind speeds and directions measured at the Isles of Shoals during the experiment are shown in Figures 3-7 and 3-8. The highest wind speeds were observed on the first day of data collection, 23 October. The appearance of breaking waves was observed at approximately 12:00 on this day. This coincided with the change in tidal current direction. After noon, the tide started to ebb, and the wind and current directions were opposing each
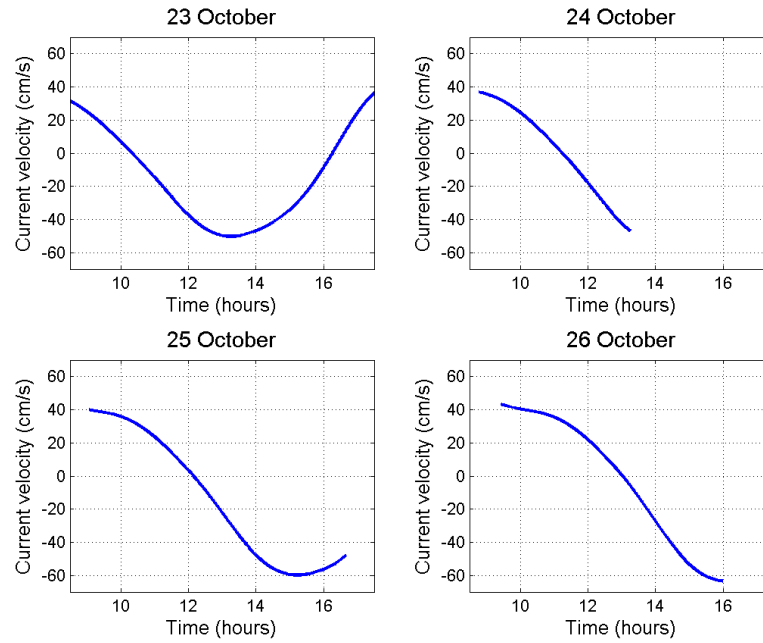
Figure 3-6: Predicted currents based on ADCP measurements gathered from May-July 2007. This plot shows the depth-averaged current velocity; negative numbers indicate ebbing currents, and positive numbers indicate flooding currents.

other.
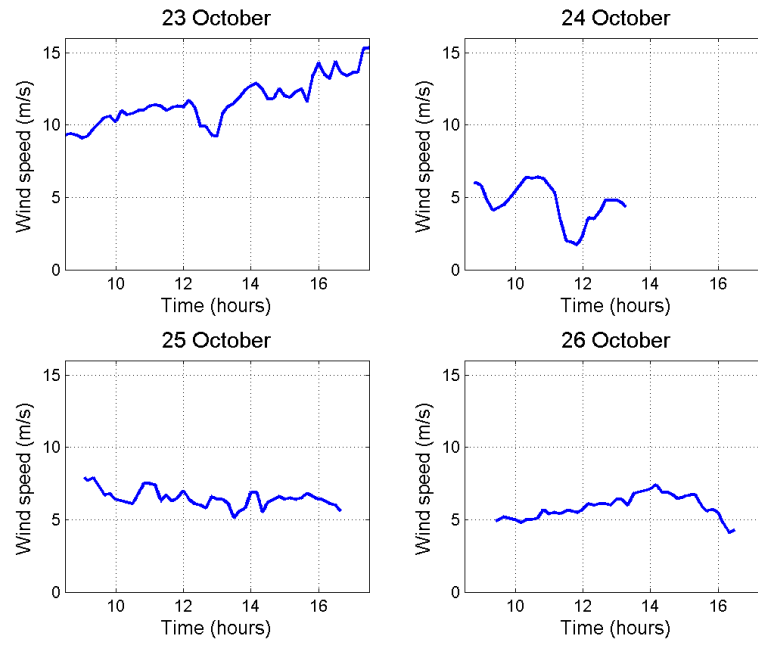
Figure 3-7: Wind speed measured at the Isles of Shoals.
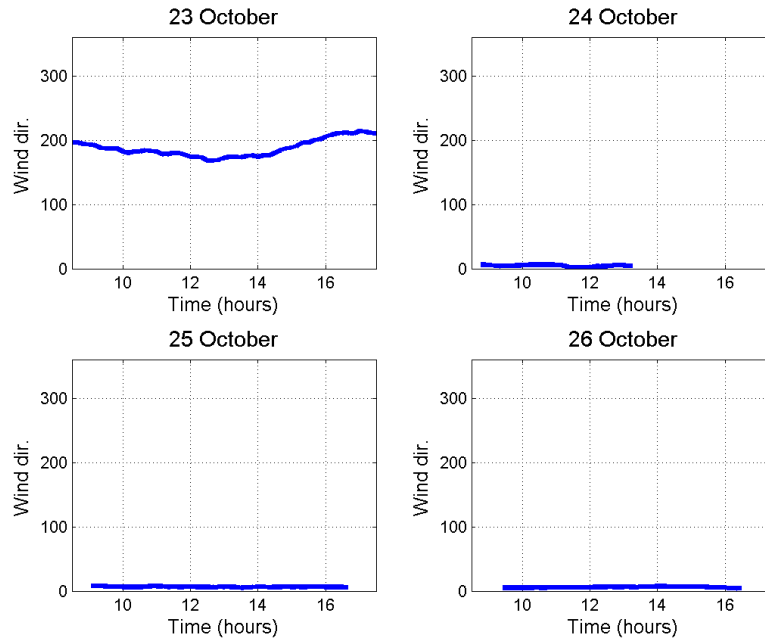
Figure 3-8: Wind direction at the Isles of Shoals, measured in degrees from true north.

3.2 Acoustic Observations

The match filtered outputs for each of the four days of data collection are shown in Figure 3-9. Sidelobes from the autocorrelation are visible. The amplitude of the first sidelobe was predicted to be 17.5 dB below the amplitude main lobe, and the separation from the first arrival was predicted to be 1.3 ms (Figure 2-6). Figure 3-9 shows the first sidelobes between 20-25 dB lower than the main arrival, and at a spacing of 1.5 ms. This discrepency in the sidelobe spacing might be a result of the fact that the received signal is a modified version of the transmitted siganl, and the cross correlation of the two is not identical to the autocorrelation of the transmitted signal. The sidelobes in the acoustic data are easily distinguishable from the main arrivals, since they are much weaker, and will follow one of the arrivals at a constant spacing.

The data also shows several occurences where the amplitude is very large for the entire sample. These events show up in the image plots as bright vertical lines, and correspond with observations of close passing lobster boats.

3.2.1 Multipath Arrival Spacing

To gain a better understanding of the multipath arrival spacing, as well as the effects of the tidal variation on the signal levels, a simple geometric model was created. The simple geometric model was designed to isolate the effects of the complex summation of the multipath arrivals as the path lengths changed with tide. It used simple boundaries: a flat bottom with constant bottom acoustic properties, a flat pressure-release surface, and a non-refracting medium. The model used a constant low-tide depth of 13 meters, a low tide transmitter depth of 9.5 meters and a low tide receiver depth of 0.5 meters. Eigenrays, or rays intersecting both the transmitter and the receiver positions were calculated using a Method of Images analysis [20]. A sketch of the model geometry is shown in Figure 3-10.

Interactions of the rays with the bottom boundary resulted in a loss in amplitude, which was computed using the magnitude of the reflection coefficient based on the incidence angle and the impedance contrast between the water and the sediment. The phase of the reflection
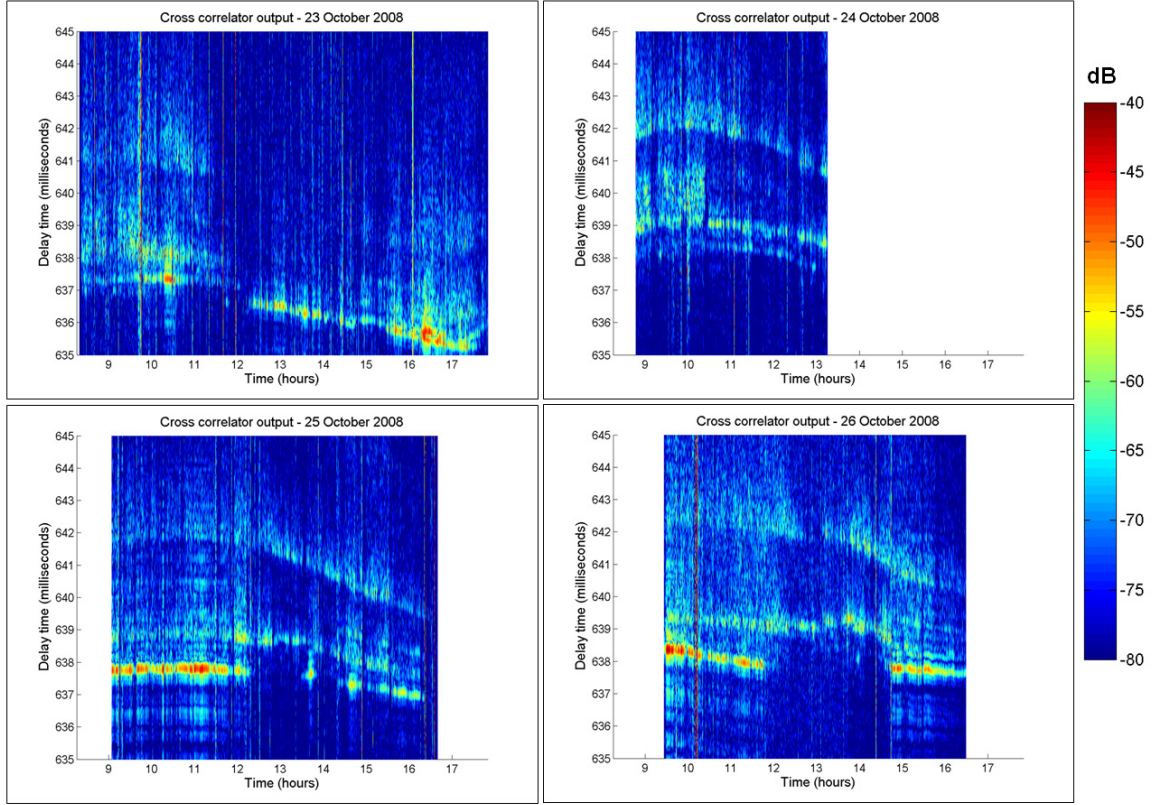
Figure 3-9: Image plots showing the amplitudes of the output of the cross correlations in decibels for each of the four days of the experiment. The image shows that for each of the received signals, several multipath arrivals might be detected. Sometimes certain arrivals appear and disappear, and their amplitudes fluctuate.

coefficient was applied as a phase shift to the transmitted signal. The properties of a course sand were used for calculation of the reflection coefficient with a sound speed in the sediment of 1836 m/s and a density of 2.034 g/cm^3 [36]. The magnitude and phase of the reflection coefficient are shown in Figure 3-11. The critical angle occurs at an incidence angle of 62°. The incidence angles for the rays that are detected at the receiver are all greater than 88°. This means that most of the energy that interacts with the bottom will be reflected, and not absorbed, except for the energy loss due to scattering from bottom roughness. The sea surface was modeled as a pressure release boundary so that interactions of the rays with
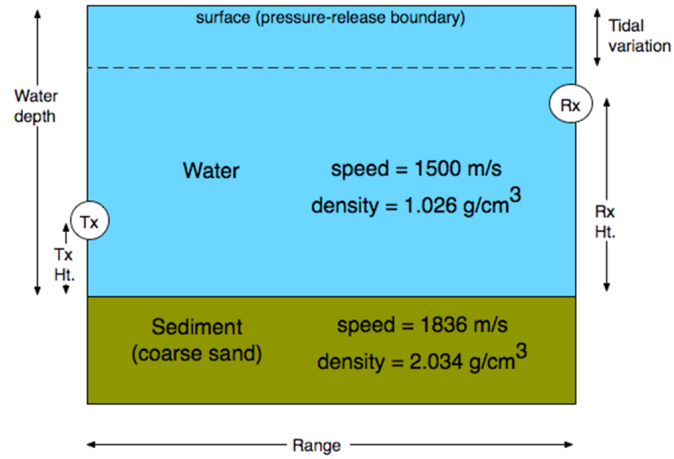
Figure 3-10: This image shows the simple geometric model that assessed the effect of the changing water levels on the received signals.

the surface resulted in a 180°phase shift.
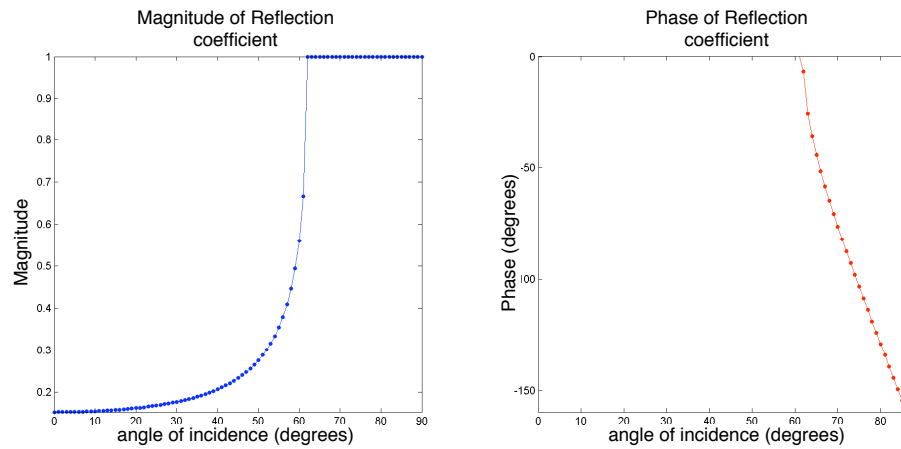
Figure 3-11: Magnitude and phase of the reflection coefficient for a rough sand and seawater interface.

The model was run at increments of tide height to observe the effect of changing depth on the signal received from the various multipath arrivals as well as to observe the spacing of the multipath arrivals. The output of the summation of received signals at changing

tide heights was processed in the same way as the signal received at the hydrophone in the experiment: it was cross-correlated with the recorded transmit signal. All of the signals used in the model were created using the sample rate used in the experiment, 100,000 samples/second. Delay times for the first few sets of multipath arrivals were considered. For example, the zeroth set is the direct path arrival, first set is the path that has had one interaction with either the surface or the bottom, and so on. In this model, the selection of the number of rays was done by comparison with the measured data. Based on the measurements, the output of the cross correlator showed the majority of the structure appearing within a window of 2-3 milliseconds. To achieve a similar spread in the model results, rays with up to eight bounces were included.

Once the rays reached the receiver, the modeled received signal retained very little resemblance to the signal that was launched in the model. An example of both the complicated arrival structure and the corresponding cross correlator output from the model are shown in Figure 3-12. As in the measured data shown above in Figure 3-9, the maximum of the cross correlation function was separated into several peaks. There were usually at least two to three distinct peaks in the autocorrelation function corresponding to different arrivals.

Since the model incorporated attenuation, rays that experienced more bounces also experienced more attenuation and had lower signal levels at the receiver. However, since these arrivals sometimes reached the receiver in phase, and sometimes out of phase, their combined effect did not always result in the first arrival being the strongest. This can be seen in the bottom plot in Figure 3-12, where the largest peak is the third peak. However, because of the attenuation, the signals did, in general, decrease in amplitude with increased arrival time, and increased number of bounces.

The simple geometric model shows that acoustic arrivals reached the receiver in closely spaced groups of four. Figure 3-13 shows the arrival times of each individual ray at each tide height. The first group of arrivals contains the direct path arrival, the surface, bottom, and bottom-surface arrivals. The grouping occurs as a result of the transmitter being very
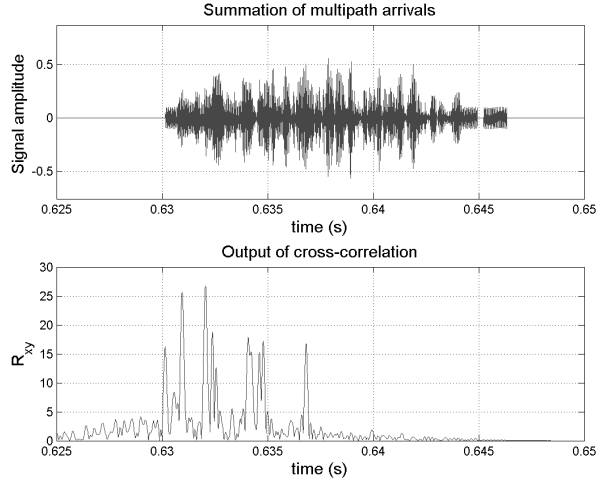
Figure 3-12: The top image shows the received signal, which contains different multipath arrivals reaching the receiver very close together in time. The bottom image shows the output of the cross correlation plotted versus delay time. Theoretically, the peak of the matched filter output should correspond with the delay time, and its amplitude should be proportional to the power in the signal.

close to the bottom and the receiver being very close to the surface, and is therefore specific to this particular source-receiver geometry. Depending on the tide height and the arrival group, the spread of arrivals within a single group varies between 0.1 - 0.5 ms. The width of main lobe from the autocorrelation was shown to be 0.128 ms. Since the spacing is most usually smaller than this, it prevents the measurement from reaching the delay-time precision predicted by the autocorrelation.

The geometry of the rays that cause these arrival groups is shown in Figure 3-14. The group that includes a direct path arrival also includes three additional arrivals that have surface or bottom bounces near the source and receiver. The proximity of the source and receiver to either a surface or bottom boundary causes the rays to be grouped.

The arrival times of each of these four groups predicts where the main peaks will occur for a given tide height. As tide height increases, any ray path that interacts with the
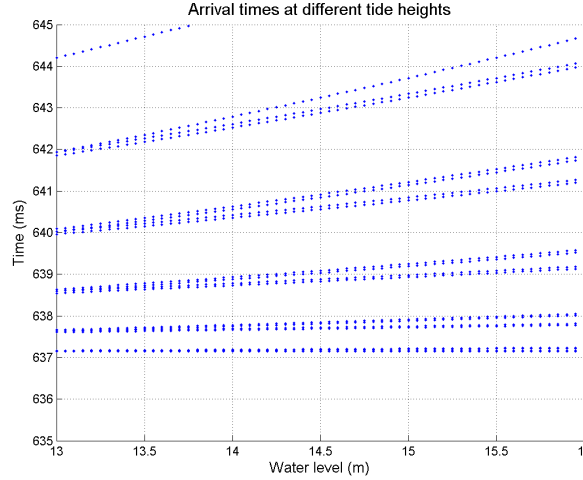
Figure 3-13: The predicted arrival times for each eigenray path are shown here. These were found using the simple geometric model. Because of this specific geometry, the arrivals appear in groups of four. The spacing of these groups increases with increasing tide height.

surface will be lengthened, and the more surface interactions that are experienced, the greater this increase in path length. This behavior can be seen in the measured acoustic data, particularly on 25 and 26 October where three main groups of arrivals are visible for large portions of the day. On 25 October, the spacing between the different arrivals is largest between approximately 10:00 and 11:00. The spacing begins to decrease significantly after 12:00. The acoustic data on 26 October shows a similar trend, except that the decrease in spacing occurs later in the day, around 13:30.

If the model's arrival time predictions are compared directly with the acoustic data on the four days, some similarities become apparent immediately. There are distinct arrivals in the acoustic data that are actually groups of arrivals that reach the receiver very close together in time. The spacing between each of the acoustically measured arrival groups also does not remain fixed. When multiple arrivals are present in the data, there is a slow variation in the spacing between them over the coarse of each day that appears consistent with the changes in tide height.

Figure 3-14: The geometry of the rays is shown in this figure, with each arrival group having a different color.

For comparison with the model, the arrival group spacing is measured at the high tide point. On 25 October, there is a high tide at 10:36am. The spacing between the first and second arrival groups at this time is 1.1 milliseconds, and the spacing between the second and third arrival groups is 2.7 milliseconds. On 26 October, the morning high tide occurs at 11:36am. The spacing between the first and second arrival groups is 1.0 milliseconds, and the spacing between the second and third arrival groups is 2.9 milliseconds. When compared with the high tide point in the model (Figure 3-13), the spacing does not match exactly. In the model, the first and second groups of arrivals at high tide are at a spacing of 0.5 ms. The second and third groups of arrivals are at a spacing of 0.9 ms. The third and fourth are at a spacing of approximately 1.2 ms. The spacing between the second and third groups (0.9 ms) is close to the spacing of the first visible arrivals in the acoustic data (1.1 ms and 1.0 ms). This might indicate that the direct path arrival is not visible in the acoustic data. However, the spacing between the third and fourth arrival groups in the model is less than half the spacing seen in the measured acoustic data. According to the model, the fourth arrival that reaches the receiver will have bounced six times from the surface and the bottom (Figure 3-14). One of the bottom bounces in this group of arrivals

33

is shown to interact with the bottom at a range of 535 m from the source. At this range, the bathymetry shows that the depth is 15 m. If this ray reached a depth of 15 m, its delay time would have been 0.51 ms longer, for a total of 1.71 ms. This indicates that fully incorporating the bathymetry would help explain the discrepency between the acoustic data and the simple geometric model.

For the remainder of this paper, the group that includes the direct path arrival will be referred to as the direct path group. The group that includes the surface-bottom bounce arrival will be referred to as the two-bounce group. The arrival that includes the surface-bottom-surface-bottom bounce will be referred to as the four-bounce arrival, and so on. The surface and bottom bounces that occur very close to the source and the receiver are not considered as bounces in this naming scheme.

The arrival structure described by the model is for a very specific source-receiver geometry. If the source or receiver are located at different heights, the arrival time spacing will change. The arrival time spacing will also change if the range between the source and receiver changes. This point is expanded upon in Appendix C, where the simple geometric model is run at different ranges and different source and receiver heights to look at the effect on arrival time spacing. These results confirm that the received arrival time structure is highly dependent on the source-receiver geometry.

3.2.2   Sound Speed Structure

Despite the similarities between the results of the simple geometry model and the acoustic data, it is also clear that the model does not fully explain the data. One of the most obvious discrepancies is the gap in the first visible group of arrivals that can be seen on 25 and 26 October (Figure 3-9). On 25 October, the first visible arrival group (the two-bounce arrival group) disappears at 12:30. It reappears briefly around 14:00, then there is a gap until just prior to 15:00. On 26 October, the signal disappears at 11:50, and does not reappear until approximately 15:00.

In Deffenbaugh's study [15], fading multipath arrivals are attributed to shallow bathymetry

34

between source and receiver, effectively blocking direct paths. The bathymetry between the source and receiver in this experiment does not change since they are both fixed. The major changes, if any, are occuring in the water column.

To look at the effect of the dynamic water column, the ray tracing program, BELLHOP [37] was run with a series of linear sound speed profiles. The first profile was iso-velocity (the same sound speed at all depths). Eigenrays were computed using the same flat surface and flat bottom geometry used in the simple model. Subsequent eigenray traces were run for increasing sound speed gradients. The linear sound speed profiles used in this simulation are shown in Figure 3-15

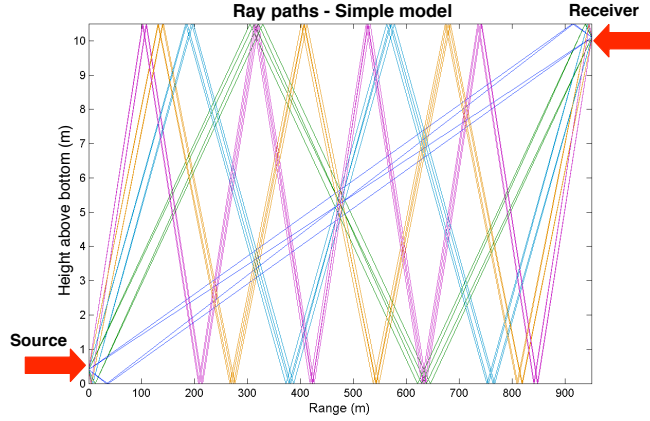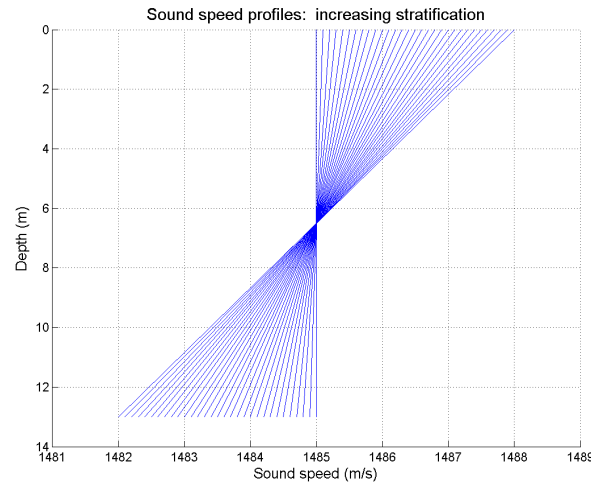
Figure 3-15: The geometry of the rays is shown in this figure, with each arrival group having a different color.

Figure 3-16 shows the results of the ray tracing. On the far left of the plot, where the gradient is less, all of the arrival groups are present, including the direct path arrival group. When the difference between the surface and bottom of the sound speed profile is greater than 0.8 m/s, the direct path arrival is no longer visible. The two-bounce arrival group also disappears when the difference between the surface and bottom sound speed reaches 4 m/s.

This analysis using the linear gradients is a useful tool in visualizing the effects of
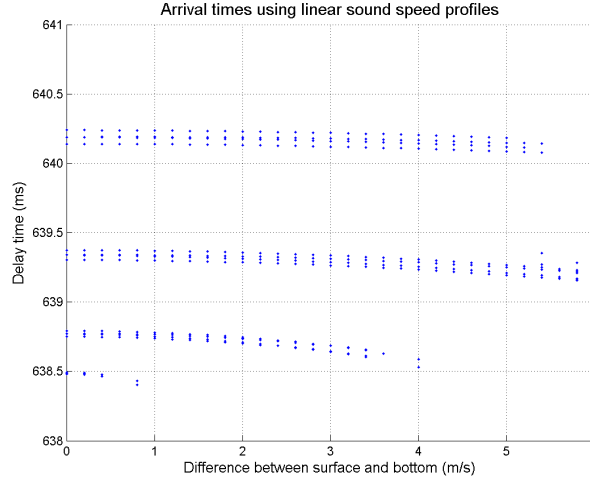
Figure 3-16: The geometry of the rays is shown in this figure, with each arrival group having a different color.

stratification; however, sound speed profiles in the harbor are not likely to be either iso-velocity or linear. Figure 3-17 shows sound speed profiles extracted from the CTD chain data on 26 October. The measured CTD chain data (Figure 3-3) shows times of relatively weak stratification, and other times when the stratification is strong. The profiles can be divided into groups based on the appearance of similar sound speed regimes in the CTD chain data. The red section are profiles between 9:05 and 11:25, where the water column is relatively well mixed. The green section are profiles from 11:25 to 13:20 where the greatest amount of stratification is observed. The magenta profiles shows a slight decrease in stratification between 13:20 and 14:05, and the blue profiles are extracted from 14:05 to the end of the day, where the water column started to become mixed again. The thicker, darker lines that overlay the individual profiles are averages for the sections. For simplicity, these four CTD chain averages will be referred to as CTD Sections 1, 2, 3, and 4, in chronological order.

In order to look at the effect of the stratification, the BELLHOP model was run with each of the four average profiles shown in Figure 3-17. The results of these four ray traces are shown in Figure 3-18.

An important point to remember when looking at these four plots is that they are based

36
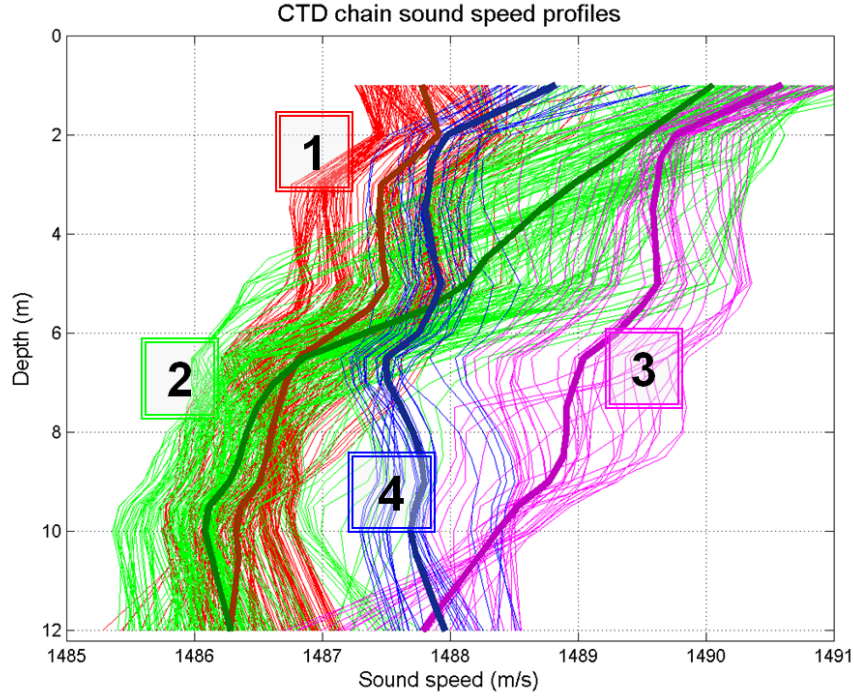
Figure 3-17: This figure shows CTD profiles extracted from the CTD chain data. The profiles are colored by sections of different sound speed profile regimes. This lines in bold show averages for each section. Section 1 is from 9:05-11:25, Section 2 is from 11:25-13:20, Section 3 is from 13:20-1405, and Section 4 is from 14:05 to the end of the day.

on a model that assumes a constant sound speed profile along the entire transect between the acoustic source and receiver, which is not the case. The sound speed profiles were often very different at separate locations along the transect, as shown in Figure 3-2. Despite this, the ray tracing results show that the different levels of stratification represented by the four CTD sections can produce very distinct ray tracing results. The weakly stratified sound speed profile average of CTD Section 1 results in a eigenray trace that does not include a direct path arrival, but does include the two-bounce group of arrivals. This matches the earlier conclusion, based on arrival spacing, that the direct path arrival does not exist in this dataset. CTD Sections 2, 3, and 4 all show similar results: that the two-bounce group of arrivals is not present, and only the four-bounce group of arrivals reaches the receiver.
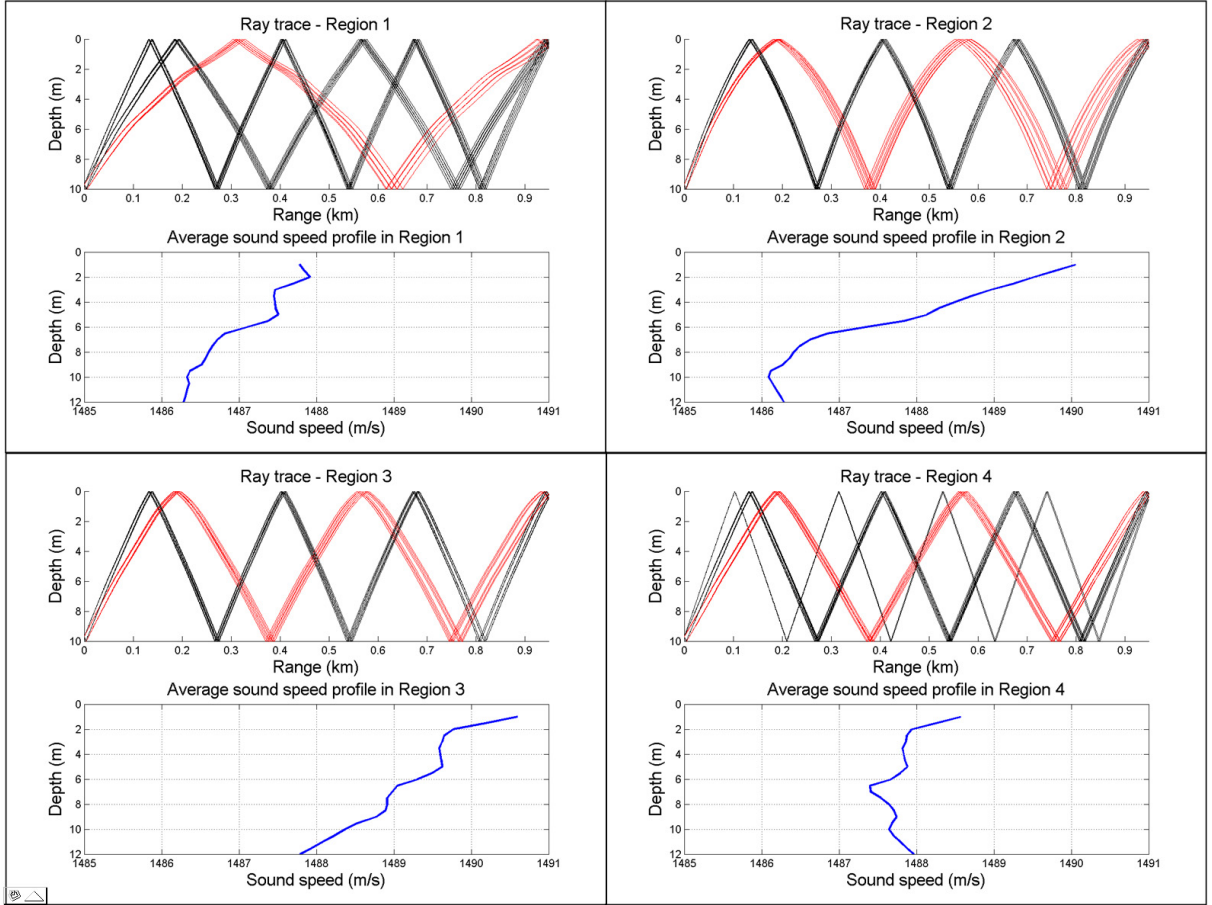
Figure 3-18: Ray traces from the four sound speed profile averages. The first arrival group to reach the receiver in each of the plots is colored in red. Section 1 - top left, Section 2 - top right, Section 3 - bottom left, Section 4 - bottom right.

CTD Section 4 is anomalous here in that it appears to be very well mixed, yet the ray tracing results show it to have a larger minimum number of bounces than CTD Section 1.

The main difference between the profile in Section 1 and the profile in Section 4 is that Section 4 shows a slight increase in sound speed at the surface. Also, the slopes of the lower 5 meters of the water column are similar in magnitude, but in opposite directions. Figure 3-19 shows the result if the same ray trace is run, except without the shallow surface layer (the top-most sound speed is changed so that it is equal to the second measurement). This figure reveals that both the direct path arrival and two-bounce arrival would in fact reach

the receiver. The first strong arrival in the acoustic data at this time shows what appears to be the two-bounce arrival. This could mean that the signal level of the direct path arrival is too low to be detected, or that the modeled sound speed profile is not fully representative of the sound speed along the travel path.
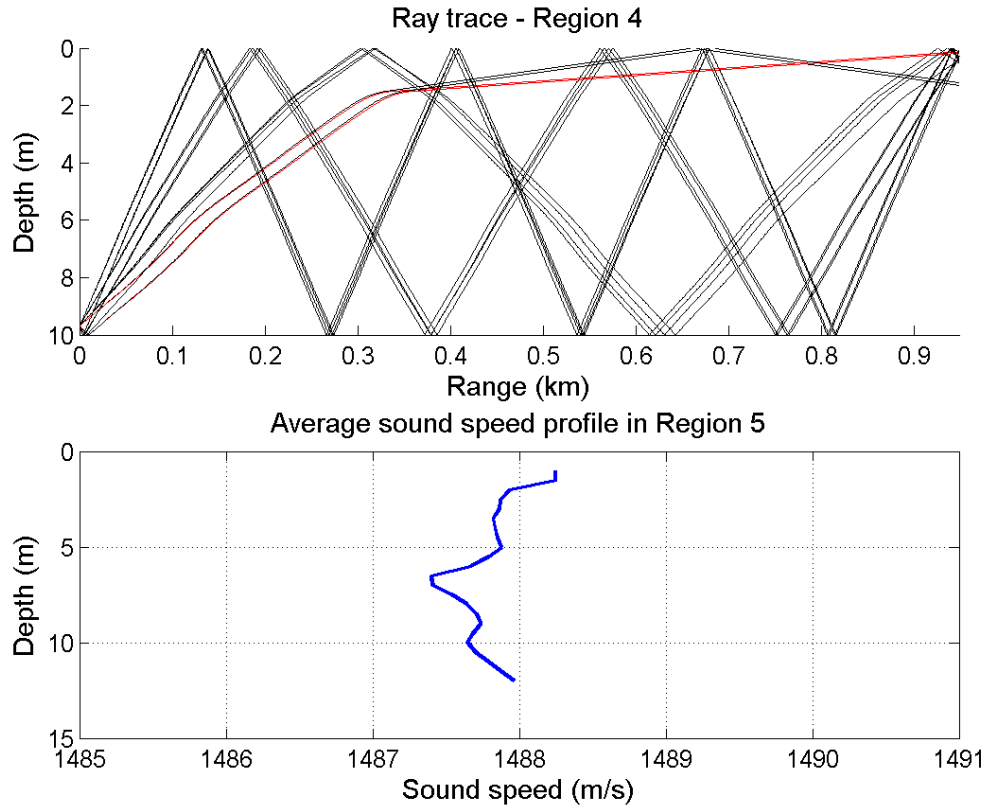
Figure 3-19: Ray trace based on sound speed profile similar to the Section 4 average, except that the top sound speed value is changed to equal the second sound speed from the top.

Grouping the CTD chain data into four sections shows the large scale effect of sound speed stratification. In order to look at the finer sound speed structure, several sound speed profiles were extracted from the CTD chain data. A total of 378 sound speed profiles from the CTD chain were used in the BELLHOP model to find the eigenrays between the source

39

and receiver. The profiles were at approximately 50 second intervals. Figure 3-20 shows the results of the eigenray trace using the CTD chain profiles. Three distinct arrivals are visible. The distinct arrivals can be seen at 10:00 at 638 ms, 638.8 ms, and 642 ms. There is a fourth, slightly blurry and intermittent arrival group that appears before the first distinct arrival. This can be seen at 10:00 at 637.5 ms. The two-bounce arrival (which is the first strong visible arrival) becomes intermittent around 11:50, and does not come back as a strong arrival until 13:30. The four-bounce arrivals remain for the entire day.
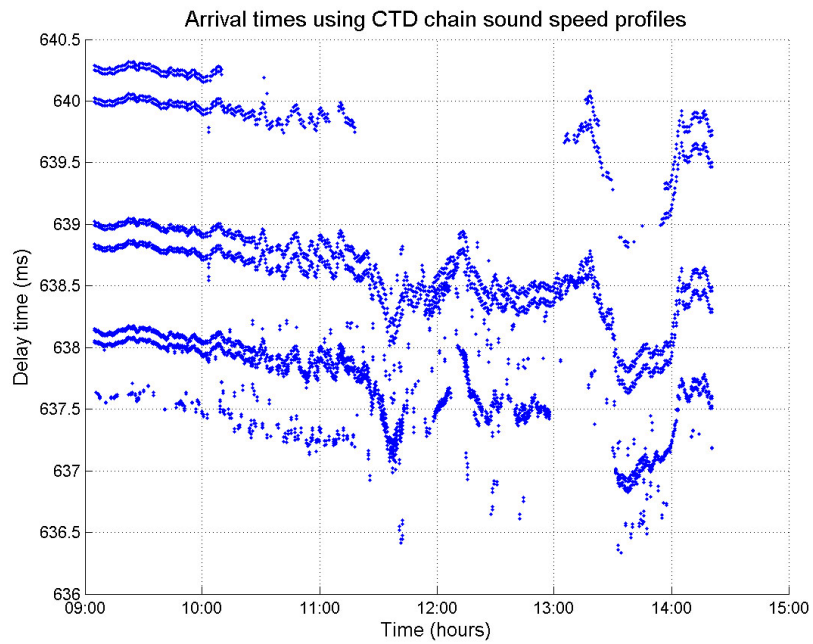
Figure 3-20: BELLHOP eigenray trace results for sound speed profiles extracted from the CTD chain data.

These results illustrate that the level of stratification can have an effect on whether a certain group of arrivals will reach the receiver or not. As a first-order approximation, the results of the CTD chain eigenray tracing confirms the conjecture that the increased stratification seen in the sound speed profiles might correspond to the gaps in the two-bounce arrival. There are three main differences between the CTD chain eigenray tracing

40

model and the acoustic data. First, the spacing of the arrivals does not match exactly. This is likely due to the fact that bathymetry was not included in the model. Some of the paths would have been slightly longer if they bounced into the deeper part of the channel. Second, the timing of the appearance and disappearance of the two-bounce arrival does not match exactly. This might be related to the fact that the CTD chain data only measures the CTD profile at one single horizontal position at any time. The Seabird CTD profiles showed that there can be significant differences in sound speed from one point along the transect to another. The third main difference that can be seen in the CTD chain eigenray trace model data are the small-scale fluctuations in arrival time, where there are arrival time changes of about 0.5 milliseconds that occur over a few minutes. The largest of these can be seen in the eigenray trace results (Figure 3-20) at 11:30, 12:15, 13:15, and 14:00. These excursions in arrival time do not appear in the acoustic data (Figure 3-9). One explanation for this is that the smaller time-scale fluctuations observed in the CTD chain data also have a small spatial extent, and are averaged out over the ray path between the source and receiver.

Although the continuous CTD chain data is not available for 23-25 October, there is additional information in the Seabird CTD profiles, the wind data, the current and the tide. On 23 October, there are only two Seabird CTD transects across the harbor, and they both occur before 12:00. The acoustic data up to this time shows the later arrivals, but the two-bounce arrival visible in the 25 and 26 October data does not appear to be present. An abrupt change happens between 11:55 and 12:05. The later arrivals disappear and what appears to be the two-bounce arrival becomes very strong. The reason that CTD casts were not collected after 12:00 on 23 October was because of increased wave action, making the Seabird CTD deployment dangerous. The wind data from the Isles of Shoals (Figures 3-7 and 3-8) shows the strongest wind speed on 23 October and it is increasing for the first part of the day. The modeled current is flooding up to slack at approximately 11:00. After this point, the ebb current is increasing, flowing south and out of the Harbor. The wind direction on this day was coming predominantly from the south, opposing the ebb flow after slack, shortly after 11:00. The opposing current and wind correspond with breaking

waves that were visible at the surface near 12:00. This combination of wind and current might have increased the amount of mixing in the channel. Uniform sound speed profiles (associated with increased mixing) have been shown to result in earlier arrivals reaching the receiver, which is consistent with the conjecture that the strong arrival seen in the second half of 23 October is the two-bounce arrival. The later arrivals have more interactions with the surface, and so will be more attenuated. Signal loss will occur as a result of bubbles just below the rough surface, as well as scattering from the rough surface itself. By 15:00 on 23 October, both the predicted current and the measured wind were decreasing, and later arrivals begin to become visible again in the acoustic data.

On 24 October, only the later arrivals are visible. The two-bounce arrivals do not appear at all on this day. The Seabird CTD chain profiles show a strongly stratified water column for the entire day. All of the profiles measured on 24 October are shown in Figure 3-21. Modeling results show that this level of stratification decreases the chances of receiving a two-bounce arrival (e.g. Figure 3-18).
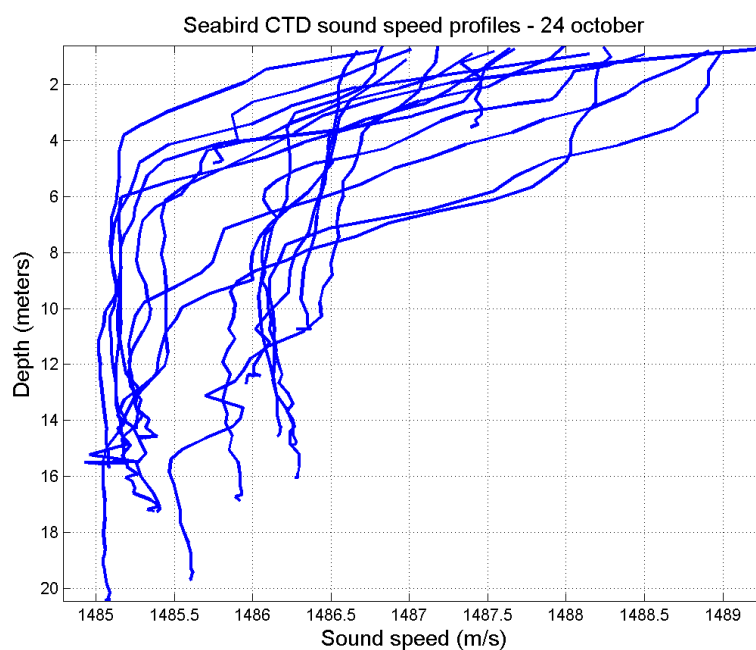
Figure 3-21: Seabird CTD sound speed profiles measured on 24 October.

The acoustic signals measured on 25 October appear very similar to those on 26 October, with three main arrival groups visible for much of the day, except for several hours during the middle of the day where the two-bounce arrival is not present (Figure 3-9. The Seabird sound speed profiles measured on 25 October appear more mixed in general than Seabird and CTD chain sound speed profiles measured on 26 October, except for the presence of a strong near surface gradient corresponding to the time when gaps in the two-bounce arrival are present (see Appendix B). This shallow surface gradient may prevent the two-bounce arrivals from reaching the receiver.

The effect of the sound speed stratification shown by the previous ray-tracing results is dependent upon the specific geometry of the source and receiver. The sound speed profiles that were measured during this experiment showed that usually the sound speed decreased with depth. This creates a downward refracting environment which has implications on the propagation between sources and receivers at certain heights. Appendix D includes examples of different source-receiver geometries and different sound speed gradients.

3.2.3   Amplitude Fluctuations

Once a signal is detected, the precision with which a time delay can be estimated using the matched filtering method is dependent on the signal to noise ratio. Burdic shows that higher precision can be achieved when estimating the location of the peak in the matched filter output if the signal to noise ratio is higher [32]. The measured signal levels, even within the two-bounce arrival group, show significant amplitude fluctuations. Figure 3-22 shows the amplitude extracted from the data on 26 October. The signal disappeared for several hours in the middle of the dataset, but on either side, the data shows fluctuations on the order of 10-30 dB. The fluctuations occur at three main time scales. There are sample-to-sample fluctuations that are on the order of seconds; slightly longer fluctuations can be seen occurring at time scales of 20-30 minutes, and there also appears to be a very low frequency signal with a period of several hours.

The simple geometric model described in Section 3.2.1 was designed to simulate the
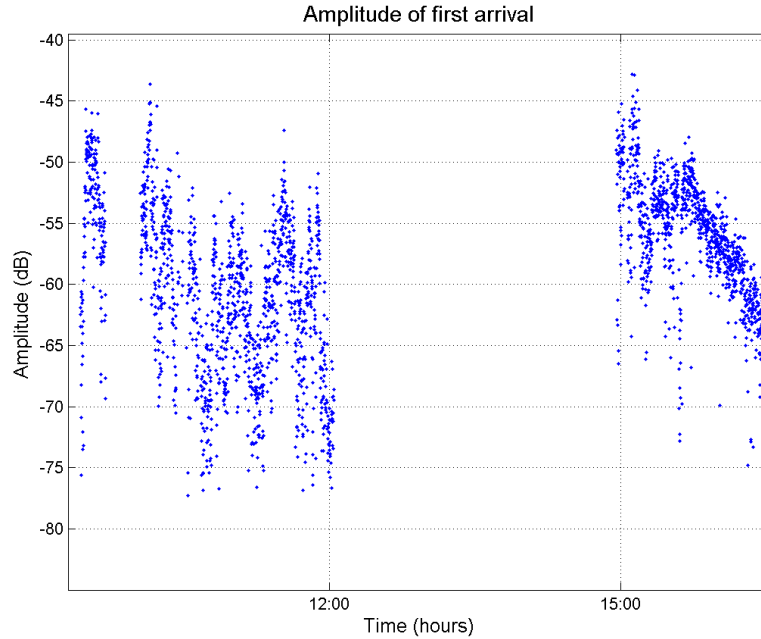
Figure 3-22: Signal amplitude extracted from the first visible arrival in the acoustic data on 26 October. The two-bounce arrival was not present from approximately 12:00 - 15:00, so this amplitude data is not shown.

relative phases of the arrival signals, so that the amplitude of the overlapping arrivals could be summed. Since the arrivals did not all reach the receiver at the same time, they sometimes would sum constructively, and sometimes destructively. One of the major ways that the tide height affected the signals was to lengthen the paths as the tide height increased, and shorten the paths as the tide height decreased. Since the different rays bounced off the surface different numbers of times, they would each be affected slightly differently as the tide height changed. The results of the simple model's amplitude analysis are shown in Figure 3-23.

The results from the simple geometric model show large amplitude fluctuations, on the order of 10 - 15 dB that have a period of approximately two hours. The amplitude and time scale of these fluctuations is similar to the low frequency fluctuations seen in the acoustic data, although the timing of the fluctuations are not predicted exactly. The high tide point

44
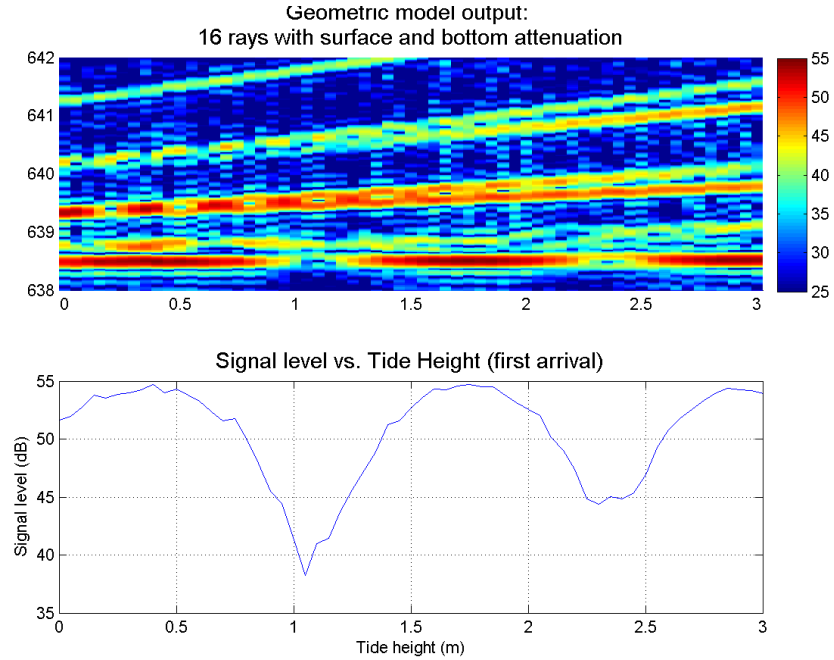
Figure 3-23: Results from the simple model amplitude analysis. The top plot shows an image of the cross correlator output at different tide heights, with colors corresponding to decibel levels. The bottom plot shows the signal level for only the first arrival extracted from the data.

in the acoustic data is at 11:36, and shows a relatively low signal, as compared with the measurements from the rest of the day. The high tide point in the model (Figure 3-23) shows a relatively high signal level. This discrepency not unexpected, since the interference pattern from the different arrivals is very sensitive to the source-receiver geometry and depth.

The high frequency fluctuations are likely influenced by the effects of inhomogeneities in the water column, the effects of surface roughness on rays that bounce off of the surface, and the effects of scattering from the bottom. When the acoustic signals travel through a medium in which there are spatial variations in sound speed at a wide range of scales, they undergo amplitude and phase modulations that accumulate along the path between the source and receiver. The effect on the measured amplitude is often referred to as

45

scintillation.

$$SI = \frac{<I^2>}{<I>^2} - 1 \qquad (3.1)$$

The scintillation of forward propagated signals in a turbulent environment was investigated by Di Iorio et al. where acoustic measurements were made across the turbulent Cordova Channel in British Columbia [38]. The average channel depth (32 m) in the Cordova Channel experiment was slightly deeper than that in the area of interest in Portsmouth Harbor (13 m), and the currents in Cordova Channel were 1 m/s, slightly stronger than the 0.67 m/s maximum currents predicted to be present in Portsmouth Harbor during the experiment. Temperature profiles measured by Di Iorio et al. showed generally weak stratification, with temperature differences within one profile rarely exceeding 0.2 degrees Celsius. This corresponds to an approximate sound speed difference of 0.8 m/s. The analysis presented in Section 3.2.2 shows that this level of stratification is relatively weak, and a direct path arrival would likely reach the receiver. In Di Iorio's experiment, the Reynold's number (the ratio of inertial to viscous forces) at maximum current was found to be 2.1×10^7, using the depth of the channel as the characteristic length scale. By comparison, the Reynold's number computed for Portsmouth Harbor was found to be 3.9×10^6. Both Reynold's numbers imply that the channels are fully turbulent at the maximum current velocity [39].

Di Iorio measured a scintillation index of 0.08 for the Cordova Channel data. The data in Portsmouth Harbor are non-stationary (Figure 3-22), so a short time series was extracted for the scintillation index calculation. The scintillation index for the Portsmouth Harbor dataset was found to be 0.47. The section used for the scintillation index was between 10:45 and 11:12 on 26 October, and is shown in Figure 3-24. The Reynolds numbers for the Cordova Channel and Portsmouth Harbor were both high, but the scintillation index for Portsmouth Harbor was much higher. This would be expected, given the much stronger temperature gradients in Portsmouth Harbor.

The acoustic rays interacting with the water surface can also affect amplitude fluctuations in the signal. As was shown in the previous sections, it is very likely that every acoustic
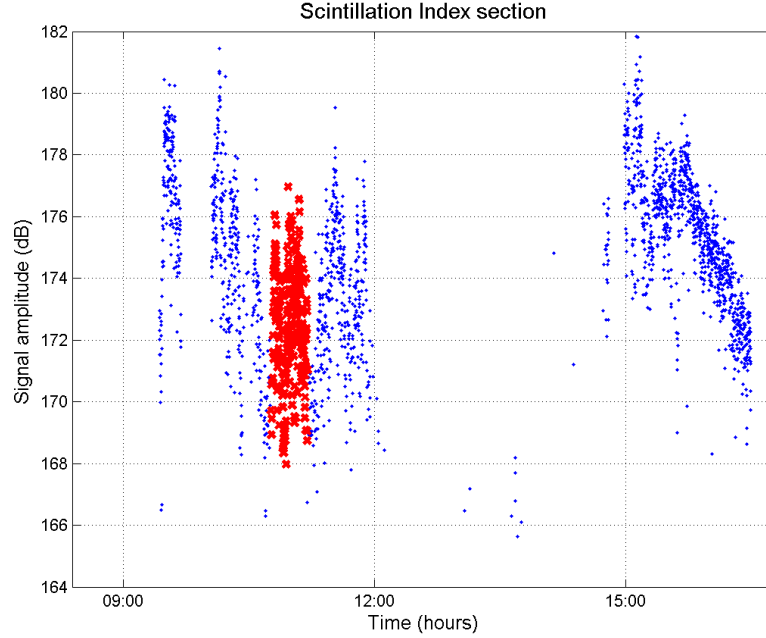
Figure 3-24: The amplitude of the received signal was non-stationary, so a smaller stationary segment of the data was selected for calculation of the scintillation index. This segment is shown in red, and it is between 10:45 and 11:12 on 26 October.

ray reaching the receiver would have interacted with the surface at least once. Each of these interactions with the surface can modulate the signal's amplitude and frequency [20]. Urick describes the effect of the surface waves on the acoustic signal. The frequency of the surface waves is shown to become superimposed on the acoustic signal.

McDaniel published a review of sea surface reverberation theories and results up to 1992 [25]. In her paper, McDaniel describes experiments that looked at backscatter strengths of signals between 3-60 kHz. Two scattering methods are found to contribute to the signal reverberation: scattering from a rough surface, and scattering from subsurface microbubbles and bubble plumes. Resonant subsurface microbubbles have the effect of scattering and attenuating the acoustic signal, and they also can change the sound speed near the surface [40]. The effect of subsurface microbubbles is difficult to predict; the effect of subsurface

microbubbles is governed by their dissolution rate, and the speed at which they rise and burst. These effects depend on the gas saturation in the surface layer, and on the temperature. Disparities in backscattering strength of an order of magnitude have been shown to exist for measurements taken under similar wind speed conditions [25]. This is consistent with the large variability observed in the Portsmouth Harbor acoustic data.

The grazing angles of the acoustic rays that are visible in the data are far less than the critical angle for the sediment-water interface, so the magnitude of the reflection coefficient will always be 1. Therefore the losses are expected to be due to scattering from the rough bottom. The amount of energy that is scattered forward and eventually reaches the receiver could vary significantly depending on precisely where the acoustic ray interacts with the bottom. The location of this interaction could change due to geometry changes in the channel caused by tide, but the ray paths geometry could be modified by changing sound speed as well.

Choi and Dahl [26] conducted a study of bottom loss in the East China Sea where acoustic sources and receivers were placed 500 meters apart. The water depth was 105 meters, and the depth of the source was at either 25 or 50 meters, and the two vertical receive arrays were at 26 and 52 meters depth. Bottom bounces were between 15 and 24 degrees, and were higher angles than those associated with the Portsmouth Harbor data. Within this range of grazing angles, the amplitude of the acoustic signals that had experienced one bottom bounce varied on the order of 5-10 dB. The scintillation index calculated for these measurements was between 0.01 and 0.2, increasing with frequency.

3.3 Range Estimates

When detecting a signal using matched filtering, the simplest approach in finding the signal's delay time is to pick the maximum peak of the cross correlation between the known transmit signal and the received acoustic signal. The location of the maximum cross correlator outputs for the Portsmouth Harbor acoustic data are shown in Figure 3-25. This figure shows the location of the peak that is picked varies widely from one ping to the next. The

amplitude of the first return frequently drops, as was seen in the amplitude fluctuations in Section 3.2.3. When this happens, the later arrivals are more likely to be picked.
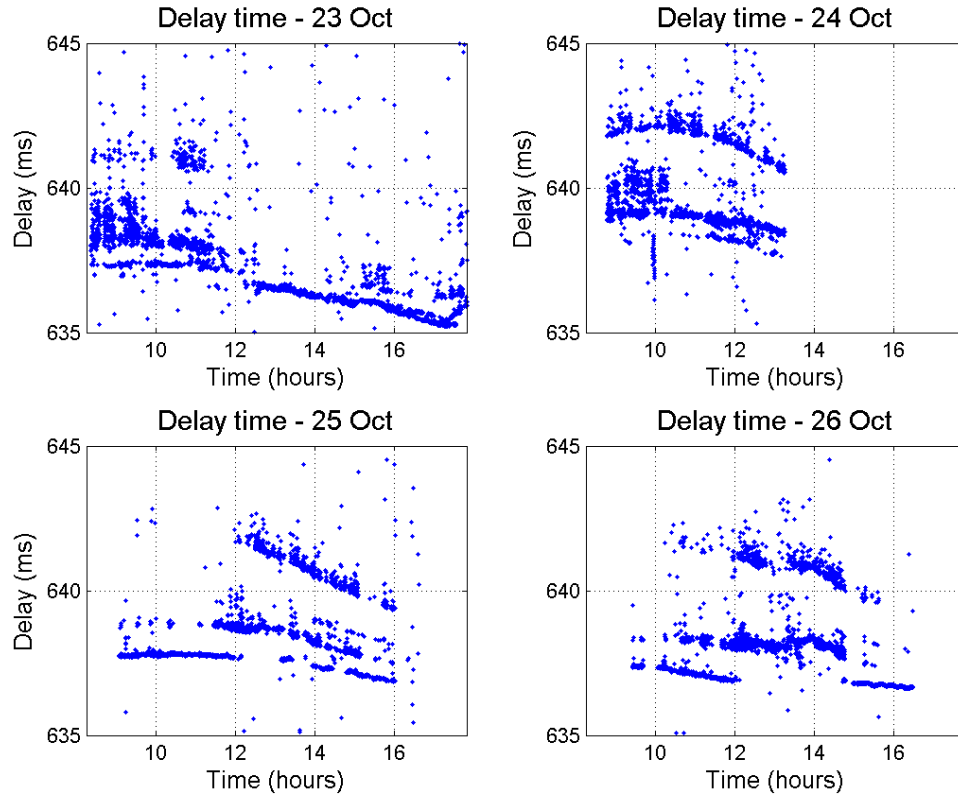
Figure 3-25: Time delays from the cross correlator output that were selected as the maximum peaks for each day of data collection. The time delay of the maximum often changes from one ping to the next, sometimes the two bounce arrival is picked, but later arrival groups are also picked

After estimating a travel time, the next step in obtaining a range is to apply an estimated sound speed along the travel path. The most continuous measure of sound speed for all four days of data collection is the Digibar sound velocimeter data (Figure 3-1). Figure 3-26 shows the travel times converted to distance using the Digibar sound velocimeter data. For comparison, the GPS-derived ranges are also shown on this plot. The GPS-derived ranges

49

are based on measurements of the source and receiver positions described in Section 2.1.

The GPS-derived ranges are consistently shorter than the shortest acoustically measured ranges by between 0.5 m and 1.9 m. There are two main reasons for this. First, the ray tracing results have shown evidence that it is unlikely that a direct path arrival ever reaches the receiver. This means that any ray that reaches the receiver has bounced at least twice, and therefore has a longer path length. Second, the Digibar sound speed data is not completely representative of the sound speed along the travel path.

Figure 3-26: This plot shows the travel times converted to distance using the Digibar sound velocimeter measurements. These acoustic distances are shown in blue. The red lines on the plots for each day are the GPS-derived range measurements between the acoustic source and receiver.

To illustrate the difference between the effect of assuming the Digibar measured sound speed, the Digibar sound velocimeter data is compared with the CTD chain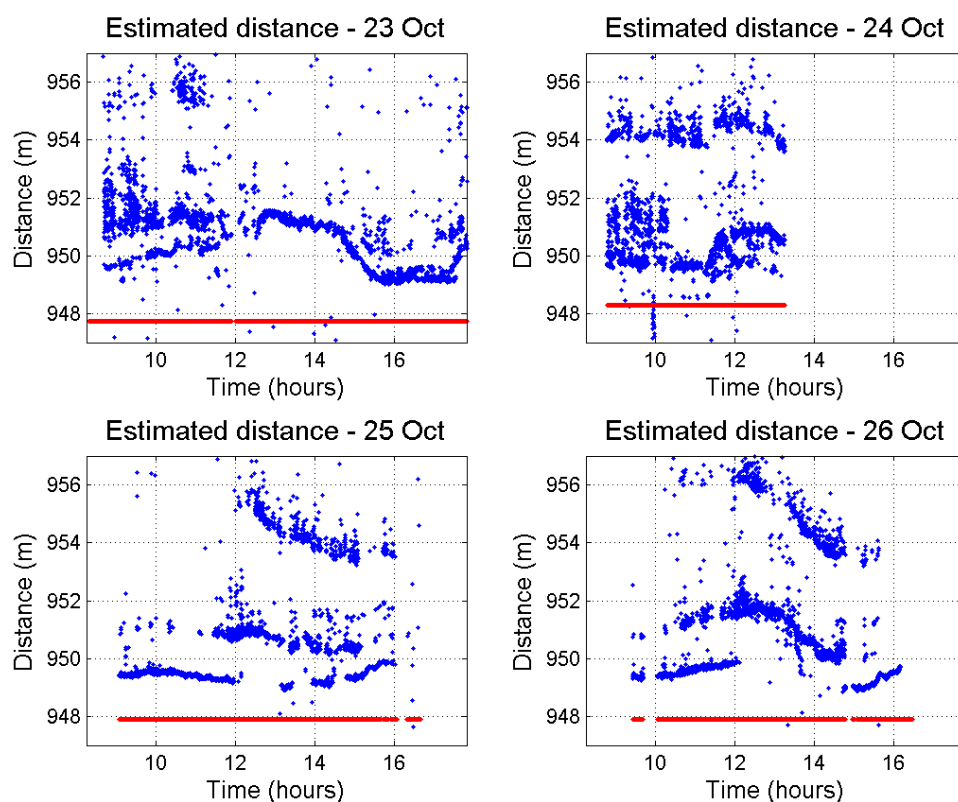 data for 26 October. Ray tracing was used to illustrate the differences between them. Sound speed profiles were extracted from the CTD chain data. These were used in the BELLHOP ray tracing program to find the arrival times of the eigenrays between the fixed source and receiver. An average depth of 10 meters was used, with the source at a depth of 9.7 meters, and the receiver at a depth of 0.5 meters. Figure 3-27 shows the results of the ray trace using sound speed profiles extracted from the CTD chain data (dark blue). The lighter blue in this plot shows the arrival times of the eigenrays computed using the digibar sound speed (with a constant velocity throughout the water column). The Digibar sound velocimeter shows consistently shorter travel times. There is some similarity in the general shape of the arrival times over the course of the day, but the Digibar ray tracing results show a much more smoothly varying arrival time, while the CTD chain data produces ray tracing results that have very rapid changes at times. This indicates higher turbulence and variability in general in the harbor, and less turbulence in the very shallow water near Fort Foster pier. Neither the CTD chain or the Digibar sound speed velocimeter was representative of the sound speed across the entire channel, however, the CTD chain data provides information about the level of stratification in the water column.

The range estimates shown in Figure 3-26 show some instances where the structure from the Digibar sound speed measurement becomes visible in the range estimates. For example, on 23 Oct at 15:00, there is a sharp decrease in the range estimate. This can be correlated with the sharp sound speed decrease occuring at the same time (Figure 3-1). Another sharp change in range can be seen at 11:30 on 24 October. This also corresponds to a rapid change in Digibar sound speed measured at the same time. Since it is unlikely that the physical range between the source and receiver was changing in this way, this indicates that the Digibar-measured sound speed is not fully representative of the sound speed fluctuations over the entire acoustic path.

The distribution of the distance estimates (using Digibar sound velocimeter data) for
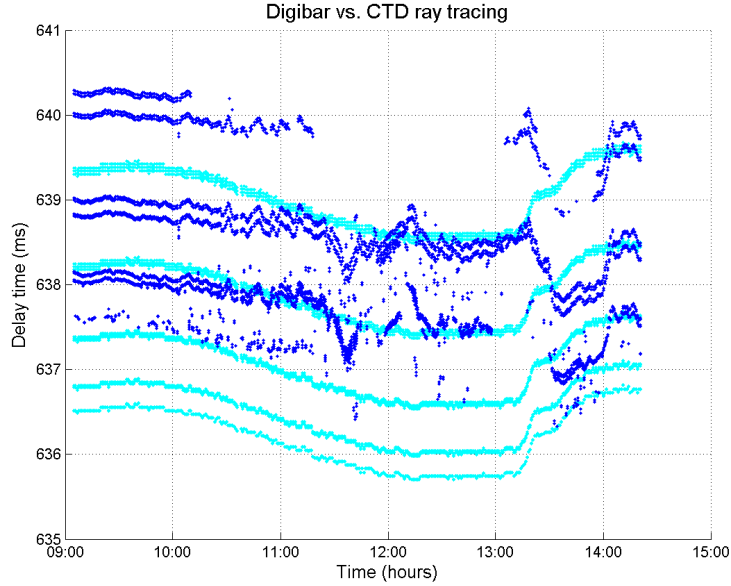
Figure 3-27: Acoustic comparison between digibar sound speed measurements and CTD chain measurements. Arrival time estimates based on ray tracing are shown.

all four days is shown in Figure 3-28. As expected, it is a multi-modal distribution, with distinct peaks corresponding to the different arrivals. The standard deviation of all detected ranges is found to be 1.85 m. The average range is 950.84 m and is skewed by 1.84 m. The data was assumed to be a superposition of three separate Gaussian distributions. Gaussian distributions were estimated by manually extracting the mean and standard deviation from the different arrival groups. The first group has a mean of 949.45 m and a standard deviation of 0.23 m. The second group has a mean of 951.07 m and a standard deviation of 0.51 m. The third group has a mean of 954.73 m and a standard deviation of 0.57 m. If the arrival groups can be associated with the peaks of this distribution, and if the bias between each group and the GPS-derived range can be estimated, then the precision of the range estimate could be improved.

The ranges measured on 25 and 26 October showed the clearest examples of the appearance of the two-bounce arrival group. Figures 3-29 and 3-30 show the two-bounce arrivals
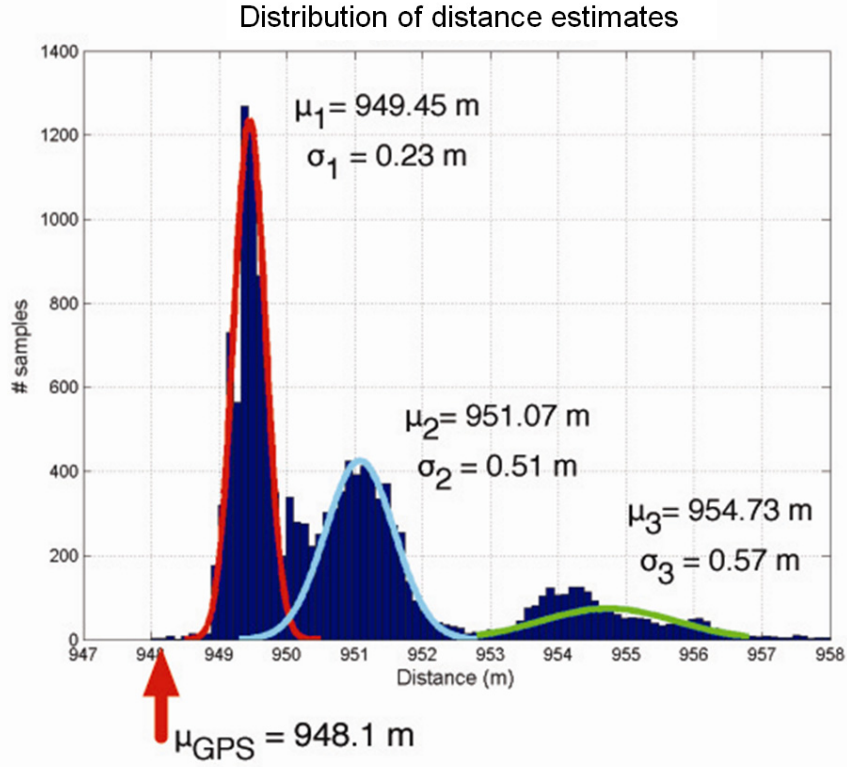
Figure 3-28: This plot shows a histogram of the distance measurements over the entire dataset. Over the individual peaks in the histogram, gaussian probability density funcitons (scaled to match the data histograms) are fitted to the data. The location of the GPS-derived measurements is shown at 948.1 m.

isolated from the later arrivals, and also histograms of the range measurements for these cases. The mean of the two-bounce arrival on 25 October is 949.43 m with a standard deviation of 0.18 m. The two-bounce arrival group on 25 October had a bias of 1.52 m from the GPS range measured on that day. The mean of the two-bounce arrival on 26 October is 949.45 m, with a standard deviation of 0.25 m. The two-bounce arrival on 26 October was, on average, 1.54 m longer than the GPS derived range.

The acoustically measured ranges are consistently longer than the GPS derived ranges between the fixed source and receiver. This is partially due to the fact that the direct path arrival is not present. Arrivals having experienced multiple bounces will have longer path

53

Figure 3-29: The two-bounce arrival is highlighted in red in the top plot, and the distribution of this arrival is shown in the bottom plot.

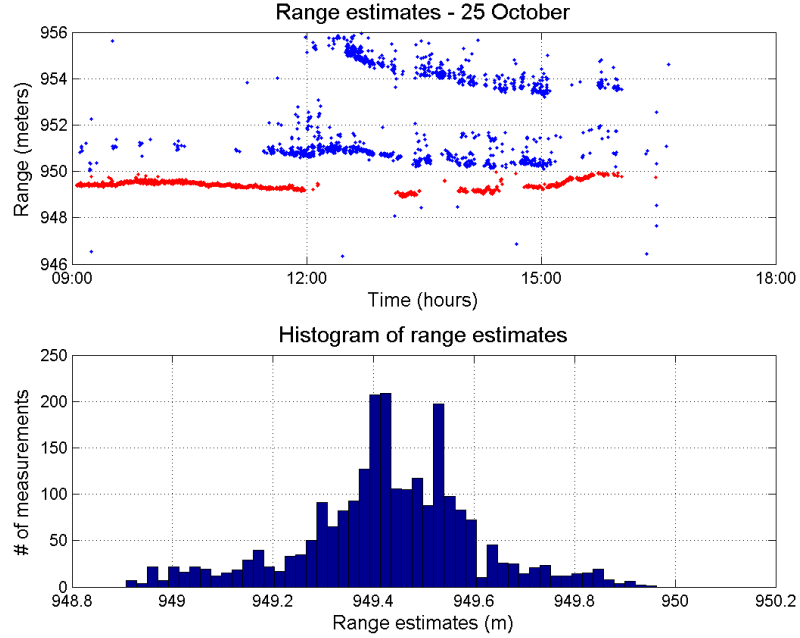lengths, and will take longer to reach the receiver. Ray tracing estimates in Figure 3-20 show an approximate delay time offset of 0.5 ms between the direct path arrival and the two-bounce arrival. This would correspond to a distance of 0.74 meters for a sound speed of 1490 m/s. The Digibar sound velocimeter provides additional data that could help explain the bias in the acoustic range. The digibar data was shown in Section 3.1 to be, on average, 1.6 m/s slower than the CTD chain data at the same depth. This would correspond to an increase in the range estimate of approximately 1 m. This is only an approximation, since estimates made using the Digibar data assume a constant sound speed along the travel path, which has been shown not to be the case. The combination of the bias in the sound speed estimate along with the lack of a direct arrival provide a possible explanation for the delay between the acoustic ranges and the GPS derived ranges.

The standard deviation of the first visible arrival group (two-bounce arrival) is 0.23 m, as compared with 0.51 m and 0.57 m for the later two arrivals. This makes sense in the
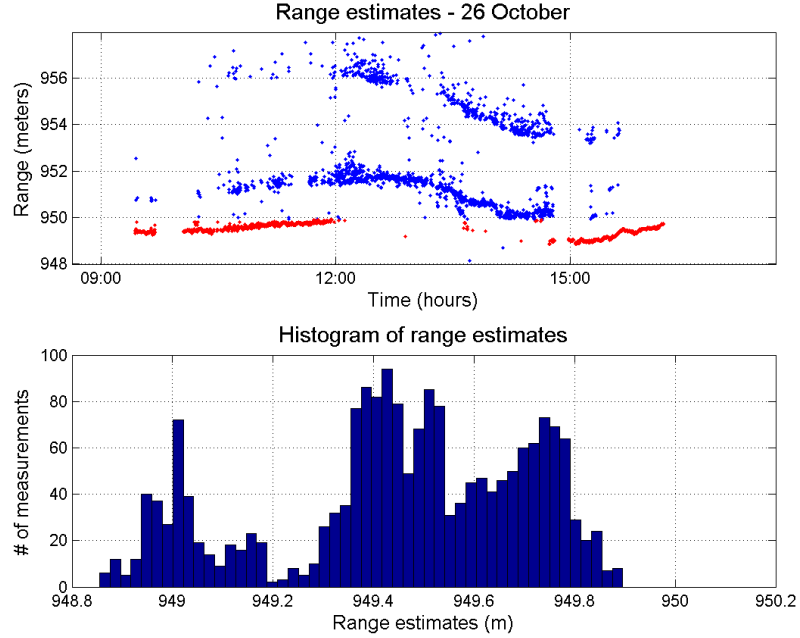
Figure 3-30: The two-bounce arrival is highlighted in red in the top plot, and the distribution of this arrival is shown in the bottom plot.

context of Burdic's description of the relationship between the signal to noise ratio and the accuracy of a matched filtering detection. Burdic shows that increased SNR results in a more precise delay detection. It is likely also related to the wider spread of range values caused by the tide for the arrivals that have experienced more surface bounces. The later arrivals in the acoustic data have decreased signal level due to the increased number of interactions with the surface and the bottom, and the spread in these range measurements is larger. Figure 3-31 shows the SNR data for all of the arrivals for all four days binned in 2 dB sections, plotted versus the standard deviation of the range measurements. The trend of this data shows the relationship between increased SNR and decreased spread in range measurements.

Figure 3-31: The standard deviation of the range measurement plotted against the signal to noise ratio. The standard deviation decreases with increases in the SNR.

CHAPTER 4

CONCLUSIONS

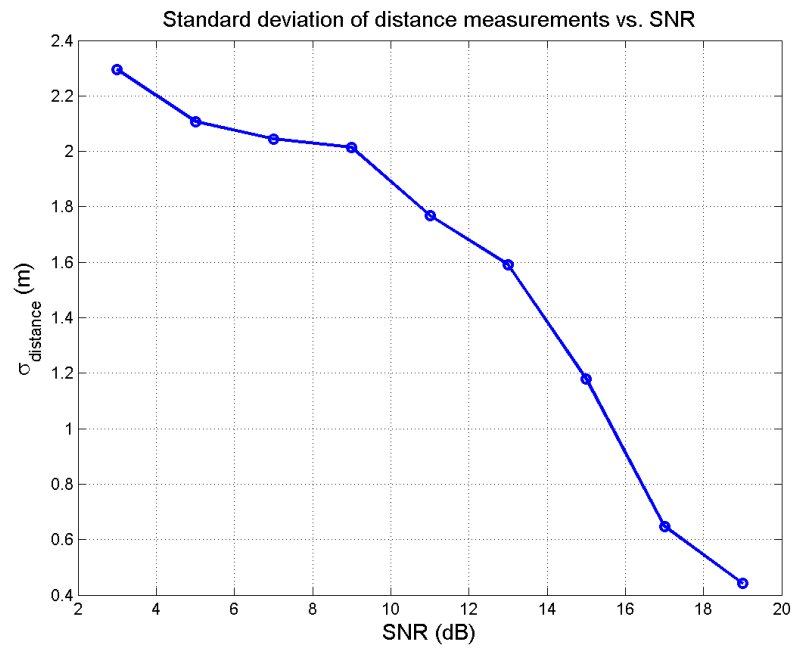This thesis has described an acoustic propagation experiment between a fixed source and a fixed receiver, spaced 948 meters apart, in an average water depth of 13 meters. The purpose of the experiment was to measure the effects of environmental variability on acoustic range measurements. Tide height, modeled current speed, wind and sound speed data were collected to gain an understanding of the physical envioronment during the experiment. This experiment was conducted from 23 October 2007 to 26 October 2007 in Portsmouth Harbor, New Hampshire.

The acoustic and environmental data collected for this experiment showed that Portsmouth Harbor is complicated, with variability in sound speed both spatially and temporally. The measured sound speed ranged from 1485 to 1495 m/s. Multipath arrivals were often visible in the data. A model based on a simplified version of the experiment geometry predicted that the arrivals would reach the receiver in groups of four, spaced closely together in time. The simple geometric model also showed that a direct path arrival is not likely, therefore the first arrival group that was detected in the acoustic data was most likely the arrival group that had experienced one surface bounce and one bottom bounce (the two-bounce arrival). The lack of a direct path arrival as well as the group arrival theory were also confirmed using ray tracing based on the simple geometry along with observed sound speed profiles. This multipath arrival structure is sensitive to the source and receiver geometry.

From an acoustic positioning perspective, it is important to understand the appearance and disappearance of the two-bounce arrival seen on 25 and 26 October. With the help of eigenray trace analysis, fading of the two-bounce arrival was attributed to the level of stratification in the water column. When the water column was weakly stratified, the

two-bounce arrival group reached the receiver. When the water column showed increased stratification, the two-bounce arrival group no longer reached the receiver, although the later arrival groups remained.

There are strong amplitude fluctuations in the data, even when a single arrival group is isolated. The sample-to-sample fluctuations in amplitude are observed to be on the order of 10-20 dB in the measured acoustic data for a single arrival group. One effect that might contribute to this is the constructive and destructive summation of the various multipath arrivals as the surface height changes. The simple geometric model used to look at this possibility showed large amplitude fluctuations, although the fluctuations were at much longer periods than what was observed in the data (several hours as opposed to a few seconds or minutes). The scintillation index was compared with that found by Di Iorio and Farmer [21] in the Cordova Channel in British Columbia. They are both relatively shallow channels, but one notable difference was that the sound speed was more uniform in the Cordova Channel, while the sound speed was, at times, very stratified in Portsmouth Harbor. The scintillation index in Portsmouth Harbor was higher than that in the Cordova Channel, despite having a smaller Reynold's number. One major difference between the two studies is that data from Portsmouth Harbor contains arrivals that have interacted with the surface and the bottom, while Di Iorio's study looks only at the direct path arrivals. Other studies ([26], [24], [41]) have shown that sea surface and seafloor roughness will both affect the amplitude fluctuations in the measured acoustic signal. The sea surface effects will depend on a number of variables including surface roughness, breaking waves and bubbles just below the surface, grazing angle, frequency of the signal, and correlation length of surface waves. The seafloor effects will also depend on several variables including bottom type, bottom roughness, grazing angle, and frequency.

The uncertainties in the acoustic range measurements arose from inadequate knowledge of the sound speed along the propagation path, as well as the uncertainty in the estimate of how many bounces a given arrival had experienced. Both of these factors affect the estimate of travel time, which in turn affects the range estimate. Despite the appearance

of multiple arrivals, the range estimates all fall within a total spread of between 5 and 8 meters, depending on the number of observed arrivals. This is less than 1 percent over the total range of 948 meters between the source and receiver. It should be noted that a robust positioning system will incorporate more than the minimum number of ranges required to uniquely define a position, providing an over-determined solution. This would enable a least squares estimation where the quality of the final position estimate is better than any of the individual range measurements.

The four- and six- bounce arrivals observed in the acoustic data could provide additional information to better estimate the true range. The approximate positions of the source and receiver, along with their ranges, provide a first-order estimate of the expected distribution of the multipath arrivals. Range estimates can be improved if arrivals can be identified and consequently corrected to the true range. This would provide sub-meter accuracy for single range measurements.

When considering schemes for LBL positioning, the most difficult aspect may be the fading of the first arrival, which is related to the overall level of stratification. To deal with this would require, at a minimum, a constant monitoring of the level of stratification present in the water column. This would provide a sense of which arrivals might be expected to be present, and could be used to help match observed arrivals with their corresponding ray paths. The spacing between multipath arrivals could also be used to help identify the different ray paths. If the multipath structure is not decoded, the most accurate range measurements will be restricted to periods of less stratification, or possibly to shorter ranges where a two-bounce arrival path is more likely, in spite of some stratification.

APPENDICES

APPENDIX A

Acoustic Source Positioning

The acoustic source in this experiment is located at a depth of approximately 10 meters, and therefore cannot be positioned using GPS. Instead, the source was acoustically positioned using a series of ranges measured between itself and a hydrophone mounted on the survey vessel (R/V Coastal Surveyor). The hydrophone on the coastal surveyor was positioned using RTK GPS. Vessel motion was measured using a POS/MV inertial motion unit and used to translate the GPS position from the GPS antenna to the hydrophone.

The range between the source and the hydrophone on the R/V Coastal Surveyor were measured acoustically. The transmit and receive times were synchronized using the 1 PPS signal from the GPS. Ranges were estimated using the average sound speed based on a Seabird CTD cast. Each range measurement from a known position defines the surface of a sphere. In theory, the spheres all intersect at the location of the unknown source. This is not usually the case, however, since there are always errors in a measurement of any kind. To solve for the unknown source position in three dimensions requires four range measurements to known positions. Each time the pinger was positioned, several hundred range measurements were collected over a span of five to ten minutes. This provided redundancy, allowing for a least squares estimate to be calculated.

The least squares estimate used here began with a simple model that describes the relationship between the source position (x_s, y_s, z_s), the receiver position (x_i, y_i, z_i), and the measured ranges (R_i), where i is the measurement number. The functional relationship between these elements is shown in Equation A.1, which implies a straight-line propagation path. This assumes that the effect of refraction due to sound speed gradients is small over the ranges being measured:

$$\sqrt{(x_i - x_s)^2 + (y_i - y_s)^2 + (z_i - z_s)^2} = R \ or \tag{A.1}$$

$$R - \sqrt{(x_i - x_s)^2 + (y_i - y_s)^2 + (z_i - z_s)^2} = 0$$

The elements that have been measured are the positions of the receiver and the ranges. These are denoted by the vector ℓ. The elements that are to be determined using the least squares estimation. These are denoted by the vector x. The general form of this functional relationship is shown in Equation A.2:

$$f(x, \ell) = 0 \tag{A.2}$$

In this case, the function f is non-linear, so Taylor's theorem is used to find a first order approximation. The first two terms of the Taylor's approximation are used (Equation A.3):

$$\mathbf{f}\left(\bar{x}, \bar{\ell}\right) = \mathbf{f}(x_o, \ell_o) + \left(\frac{\partial \mathbf{f}}{\partial x}\right)_o (\bar{x} - x_o) + \left(\frac{\partial \mathbf{f}}{\partial \ell}\right)_o \left(\bar{\ell} - \ell_o\right) \tag{A.3}$$

where x_o and ℓ_o are initial approximations, and $\bar{x}$ and $\bar{\ell}$ are the true values of the measurements and the parameters. Since we are dealing with vector quantities of measurements, parameters and also functional equations, the Jacobian matrix of the coefficients must be calculated ([42], [31]):

$$\frac{\partial \mathbf{f}}{\partial \mathbf{x}} = \begin{bmatrix} (\partial f_1/\partial x_1) & (\partial f_1/\partial x_2) & \dots & (\partial f_1/\partial x_u) \\ (\partial f_2/\partial x_1) & (\partial f_2/\partial x_2) & \dots & (\partial f_2/\partial x_u) \\ \vdots & \vdots & & \vdots \\ (\partial f_c/\partial x_1) & (\partial f_c/\partial x_2) & \dots & (\partial f_c/\partial x_u) \end{bmatrix} = \mathbf{A} \tag{A.4}$$

where u is the number of elements to be estimated by the least squares process, and c is the number of functions. This is sometimes called the design matrix. A second Jacobian matrix must be calculated as well. This one involves the partial derivatives of the measured values, ℓ:

$$\frac{\partial \mathbf{f}}{\partial \boldsymbol{\ell}} = \begin{bmatrix} (\partial f_1/\partial \ell_1) & (\partial f_1/\partial \ell_2) & \ldots & (\partial f_1/\partial \ell_m) \\ (\partial f_2/\partial \ell_1) & (\partial f_2/\partial \ell_2) & \ldots & (\partial f_2/\partial \ell_m) \\ \vdots & \vdots & & \vdots \\ (\partial f_c/\partial \ell_1) & (\partial f_c/\partial \ell_2) & \ldots & (\partial f_c/\partial \ell_m) \end{bmatrix} = \mathbf{B} \tag{A.5}$$

where m is the number of measured elements. The partial derivatives with respect to each of the elements of x and ℓ are evaluated in Equations A.6 - A.12:

$$\frac{\partial f}{\partial x_i} = -\frac{x_i - x_s}{\sqrt{(x_i - x_s)^2 + (y_i - y_s)^2 + (z_i - z_s)^2}} \tag{A.6}$$

$$\frac{\partial f}{\partial y_i} = -\frac{y_i - y_s}{\sqrt{(x_i - x_s)^2 + (y_i - y_s)^2 + (z_i - z_s)^2}} \tag{A.7}$$

$$\frac{\partial f}{\partial z_i} = -\frac{z_i - z_s}{\sqrt{(x_i - x_s)^2 + (y_i - y_s)^2 + (z_i - z_s)^2}} \tag{A.8}$$

$$\frac{\partial f}{\partial R} = 1 \tag{A.9}$$

$$\frac{\partial f}{\partial x_s} = \frac{x_i - x_s}{\sqrt{(x_i - x_s)^2 + (y_i - y_s)^2 + (z_i - z_s)^2}} \tag{A.10}$$

$$\frac{\partial f}{\partial y_s} = \frac{y_i - y_s}{\sqrt{(x_i - x_s)^2 + (y_i - y_s)^2 + (z_i - z_s)^2}} \tag{A.11}$$

$$\frac{\partial f}{\partial z_s} = \frac{z_i - z_s}{\sqrt{(x_i - x_s)^2 + (y_i - y_s)^2 + (z_i - z_s)^2}} \tag{A.12}$$

The coefficients of these Jacobian matrices are evaluated at the initial approximations x_o and ℓ_o. When Equation A.4 and Equation A.5 are substituted into Equation A.3 (where $\mathbf{f}(x_o, \ell) = 0$), it results in:

$$\boldsymbol{f}(x_o, \ell) + \boldsymbol{A}(\bar{x} - x_o) + \boldsymbol{Bv} = 0 \tag{A.13}$$

where v is the vector of residuals, $\bar{\ell} - \ell_o$. The term residuals may be misleading, because these are not really something that is left over. The residuals vector actually contains the corrections that are to be applied to the the measured values in order to meet the least squares criteria [31].

If we then substitute x for $(\bar{x} - x_o)$, and b for $-f(x_o, \ell)$, we arrive at Equation A.14. This is the matrix representation of the functional relationship once it has been linearized.

$$Ax + Bv = b \tag{A.14}$$

The basic concept of least squares is to minimize the sum of the squared residuals [43]. The residuals are weighted by W, which is the weight matrix of ℓ. Equation A.15 shows the function that must be minimized.

$$\phi = v^t W v \tag{A.15}$$

Some problems are constructed in such a way that a simpler version of least squares may be used. For example, if each equation in the functional model f contains only one measured value, the *observation equations* method may be used. Another example is if the vector of unknowns x does not appear in the functional model. Unfortunately, our problem does not fall into either of these categories, so we must carry out the more rigorous *general least squares* method Cooper [31].

Since the general least squares method is being used here, Lagrangian multipliers k must be used. These are necessary since we are looking for solution by a constrained minimum, where there are as many multipliers k_i as there are constraints [44]. The Lagrange multipliers are incorporated into the solution as follows:

$$\phi = v^t W v + 2k^t (Ax + Bv - b) \tag{A.16}$$

The Lagrange multiplier is multiplied by a factor of two in order to simplify further calculations. In order to minimize ϕ, the partial derivatives of ϕ with respect to both x and v must be set to zero (Equations A.17 and A.18).

$$\frac{\partial \phi}{\partial \boldsymbol{x}} = 2\hat{\boldsymbol{k}}^t \boldsymbol{A} = 0 \tag{A.17}$$

$$\frac{\partial \phi}{\partial \boldsymbol{v}} = 2\hat{\boldsymbol{v}}\boldsymbol{W} + 2\hat{\boldsymbol{k}}^t \boldsymbol{B} = 0 \tag{A.18}$$

Combining and re-arranging Equations A.14, A.17, and A.18 results in estimate of $\hat{\boldsymbol{x}}$.

$$\hat{\boldsymbol{x}} = \left[\boldsymbol{A}^t(\boldsymbol{B}\boldsymbol{W}^{-1}\boldsymbol{B}^t)\right]^{-1} \boldsymbol{A}(\boldsymbol{B}\boldsymbol{W}^{-1}\boldsymbol{B}^t)^{-1}\boldsymbol{b} \tag{A.19}$$

The expression for the least squares residuals, $\hat{\boldsymbol{v}}$, is given in Equation A.20. This can be used as corrections to the initial approximations before carrying out further iterations.

$$\hat{\boldsymbol{v}} = \boldsymbol{W}^{-1}\boldsymbol{B}^t(\boldsymbol{B}\boldsymbol{W}^{-1}\boldsymbol{B}^t)^{-1}$$
$$\times \left\{\boldsymbol{I} - \boldsymbol{A}[\boldsymbol{A}^t(\boldsymbol{B}\boldsymbol{W}^{-1}\boldsymbol{B}^t)^{-1}\boldsymbol{A}]^{-1}\boldsymbol{A}^{-1}(\boldsymbol{B}\boldsymbol{W}^{-1}\boldsymbol{B}^t)^{-1}\right\}\boldsymbol{b} \quad (A.20)$$

Figure A-1 shows the ranges measured by the survey vessel (R/V Coastal Surveyor) as it maneuvered around the pinger position. This example shows the measurements collected on 25 October. The pinger was positioned acoustically once on 23 October, twice on 24 October, and once on 25 October.

The solutions for each of these acoustically derived positions are listed in Table A.1, along with the corresponding standard deviations that were extracted from the covariance matrix from the least squares estimation. The positions are shown graphically in Figure A-2.

The law of propagation of variances is used to propagate uncertainties in the positions of the source and receiver to the uncertainty in the derived range estimate [44]. The range R is a non-linear function of the measurements of the bottom-mounted pinger position (x_p, y_p, and z_p) and the receiver position (x_r, y_r, and z_r). This functional relationship is shown in Equation A.21. For simplicity, the measurements are assumed to be independent.

$$R = \sqrt{(x_p - x_r)^2 + (y_p - y_r)^2 + (z_p - z_r)^2} \tag{A.21}$$
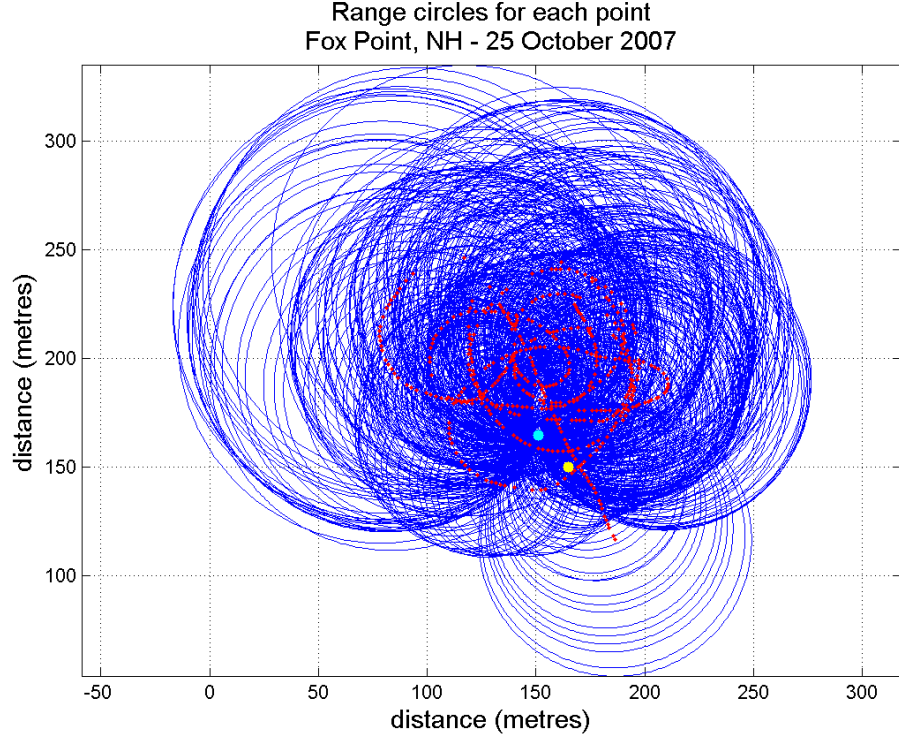
Figure A-1: For each position of the R/V Coastal Surveyor (red dots), a range was measured between the bottom-mounted pinger, and the hydrophone on the ram of the vessel. Two-dimensional versions of these ranges are shown by the blue circles. An initial position estimate is shown by the yellow dot, and the final position estimate is shown by the light blue dot.

The standard deviation of R is found by first computing the variance (Equation A.22).

$$\sigma_R^2 = \left(\frac{\partial R}{\partial x_p}\right)^2 \sigma_{x_p}^2 + \left(\frac{\partial R}{\partial y_p}\right)^2 \sigma_{y_p}^2 + \left(\frac{\partial R}{\partial z_p}\right)^2 \sigma_{z_p}^2 + \left(\frac{\partial R}{\partial x_r}\right)^2 \sigma_{x_r}^2 + \left(\frac{\partial R}{\partial y_r}\right)^2 \sigma_{y_r}^2 + \left(\frac{\partial R}{\partial z_r}\right)^2 \sigma_{z_r}^2$$

(A.22)

The standard deviations in range for each of the pinger positioning exercises are shown in Table A.2.

Date	Northing	σ_N	Easting	σ_E
23 October	4769765.90	0.087	360996.36	0.094
24 October (a)	4769762.07	0.140	360995.09	0.061
24 October (b)	4769762.07	0.050	360995.16	0.050
25 October	4769764.59	0.057	360995.93	0.052

Table A.1: Acoustically derived positions of the bottom-mounted pinger, along with the standard deviations of the northing and easting estimates (all measurements in meters).

Date	Range	σ_R
23 October	947.760	0.109
24 October (a)	948.324	0.086
24 October (b)	948.255	0.075
25 October	947.946	0.076

Table A.2: Range measurements along with standard deviations in meters.
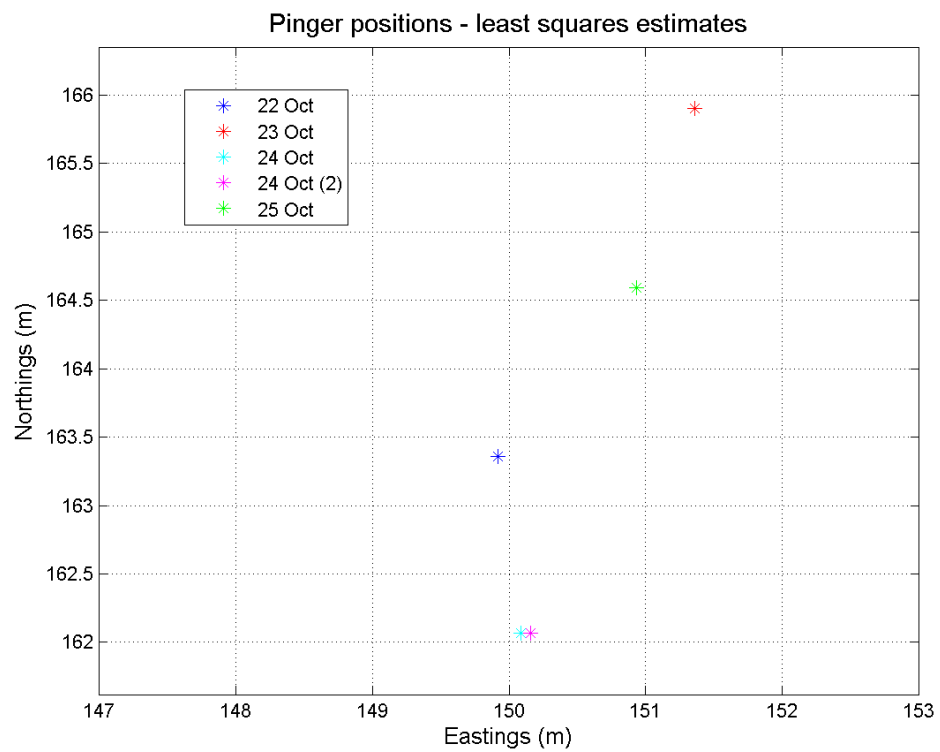
Figure A-2: Acoustically derived pinger positions.

APPENDIX B

CTD plots

The following plots show all of the Seabird CTD profiles measured over the course of the acoustic data collection. These profiles were collected along the profile between the source and receiver. In each of these plots, the chart is on the top left, with colored dots corresponding to the colors of the CTD profiles shown in the top right plot. The bottom plot shows the tide height at the measurement point. The bottom figure shows the tide height at the measurement time.
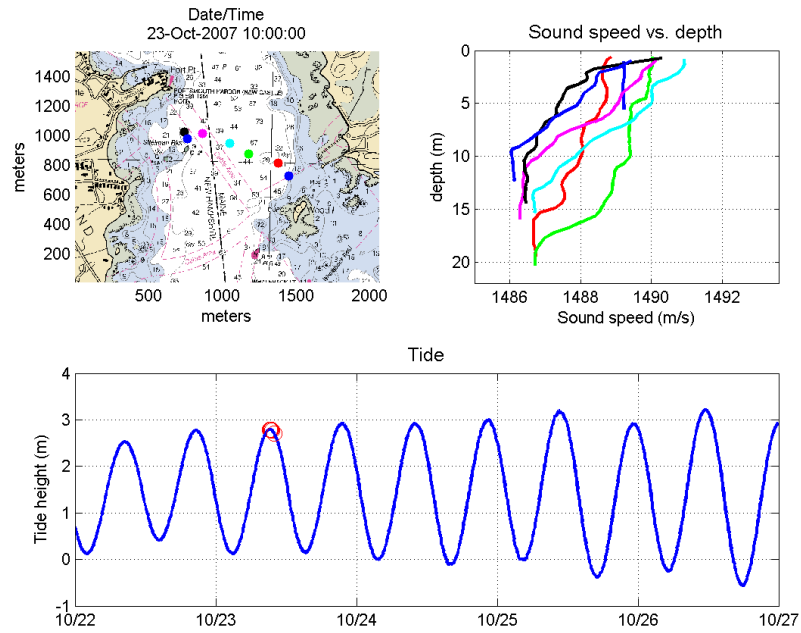
Figure B-1: Sound speed transect 23 October 2007 at 10:00.
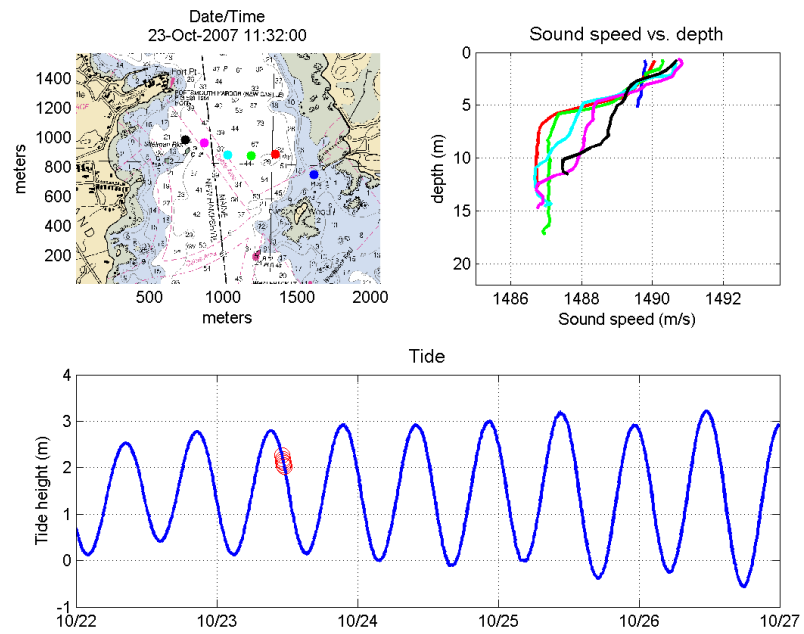
Figure B-2: Sound speed transect 23 October 2007 at 11:32.
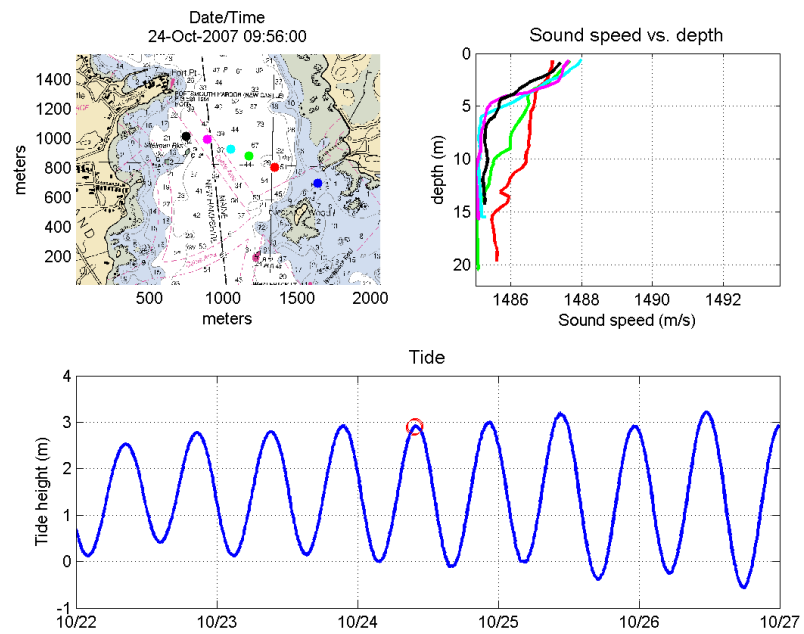
Figure B-3: Sound speed transect 24 October 2007 at 9:56.
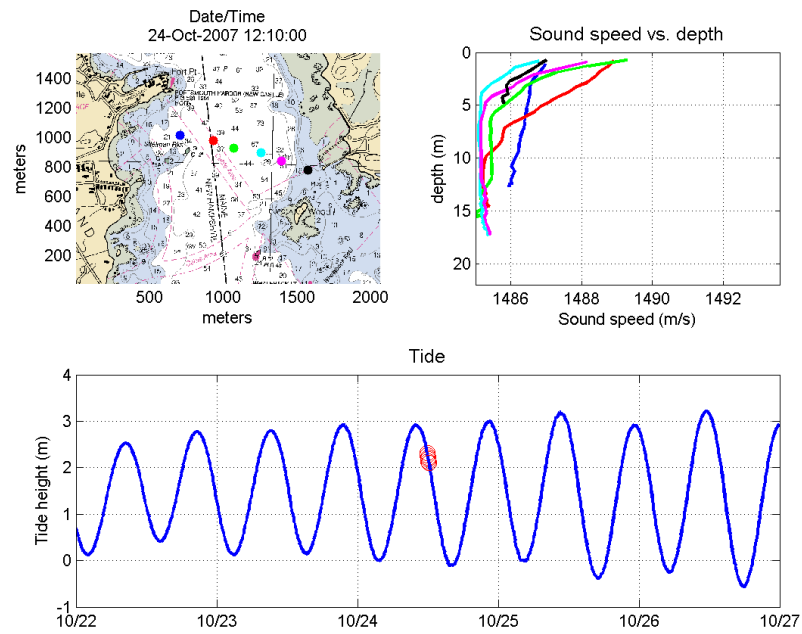
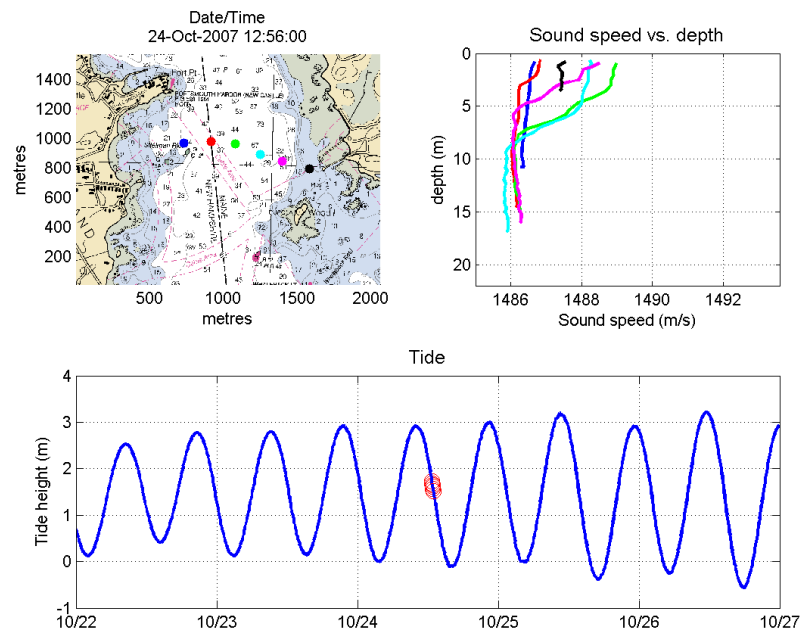Figure B-4: Sound speed transect 24 October 2007 at 12:10.

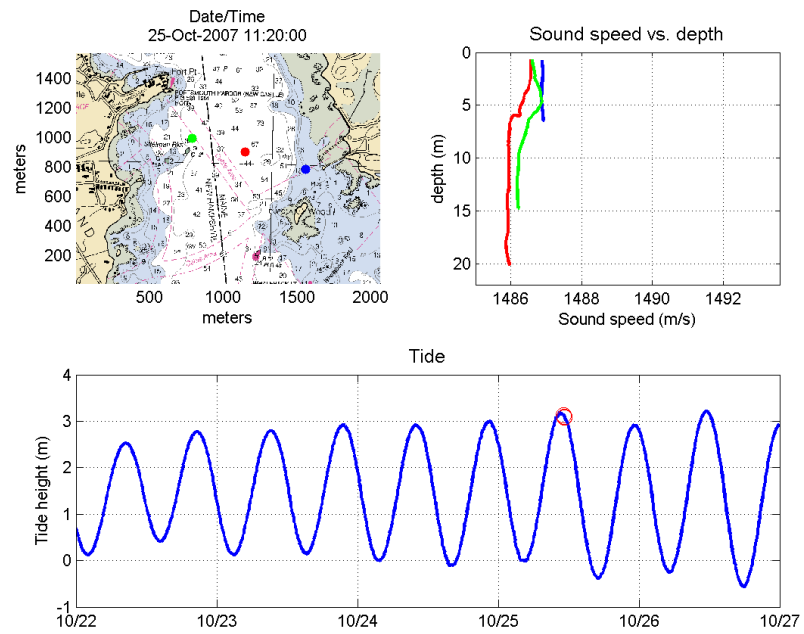Figure B-5: Sound speed transect 24 October 2007 at 12:53.

71

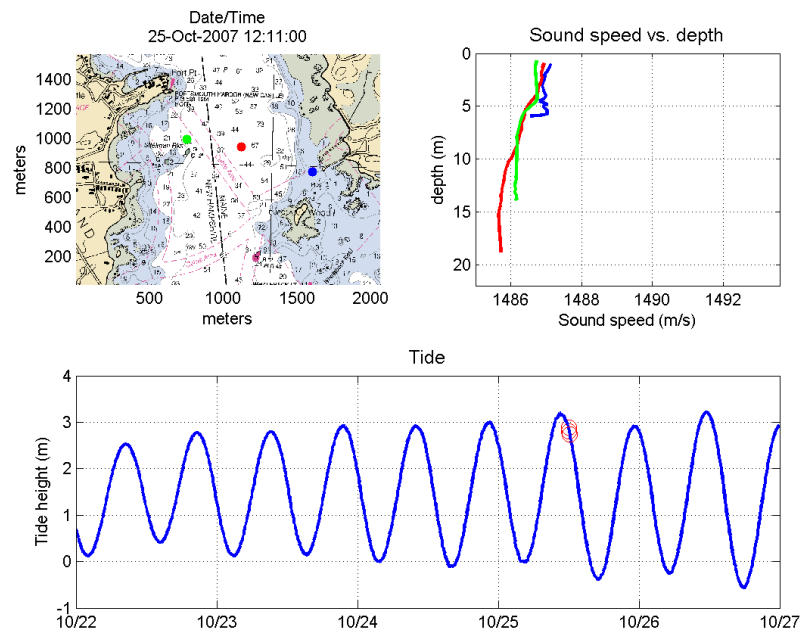Figure B-6: Sound speed transect 25 October 2007 at 11:20.

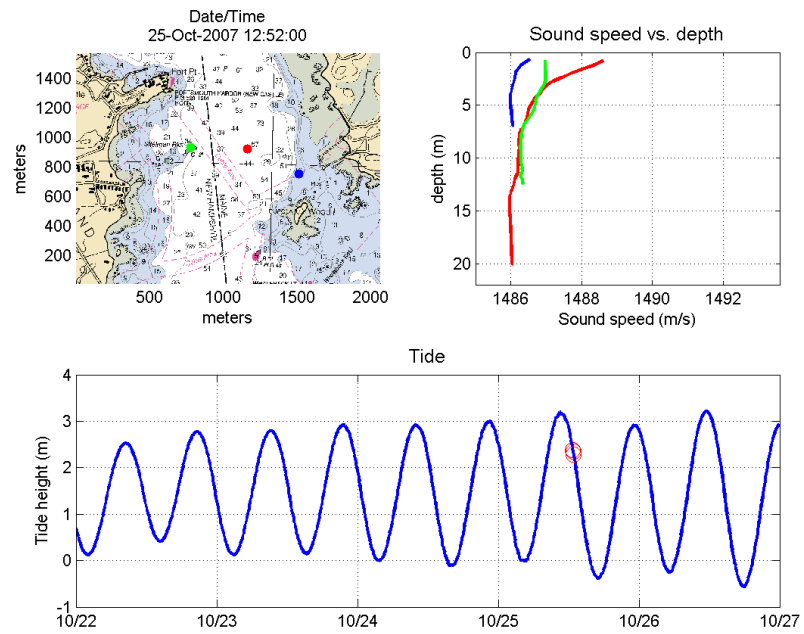Figure B-7: Sound speed transect 25 October 2007 at 12:11.

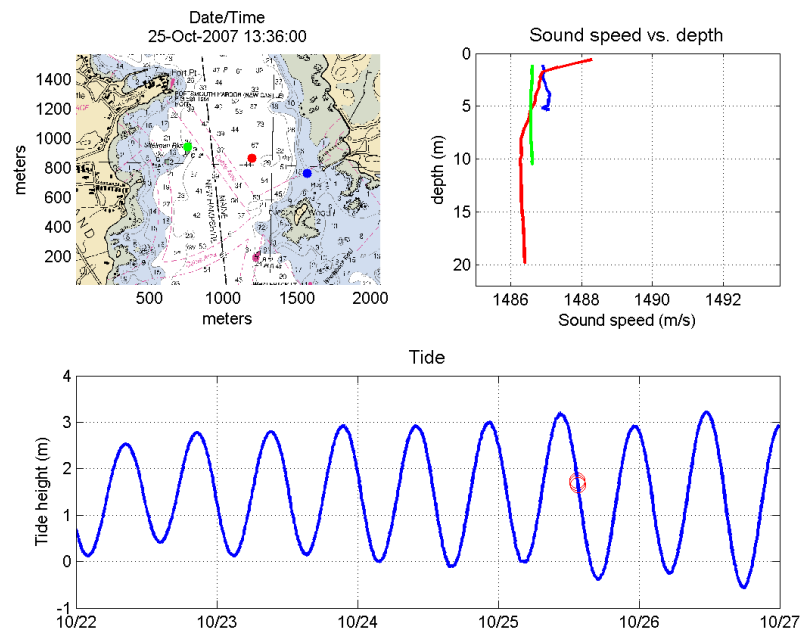Figure B-8: Sound speed transect 25 October 2007 at 12:52.

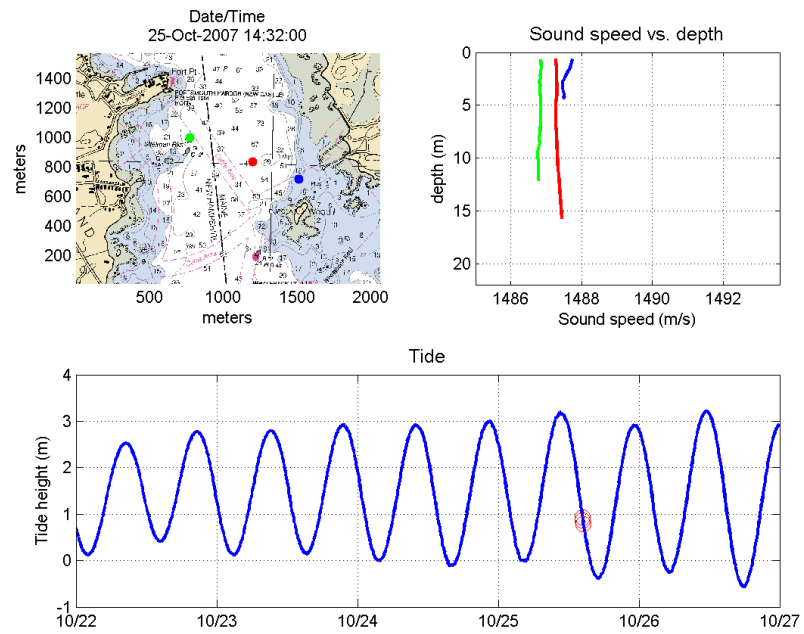Figure B-9: Sound speed transect 25 October 2007 at 13:36.

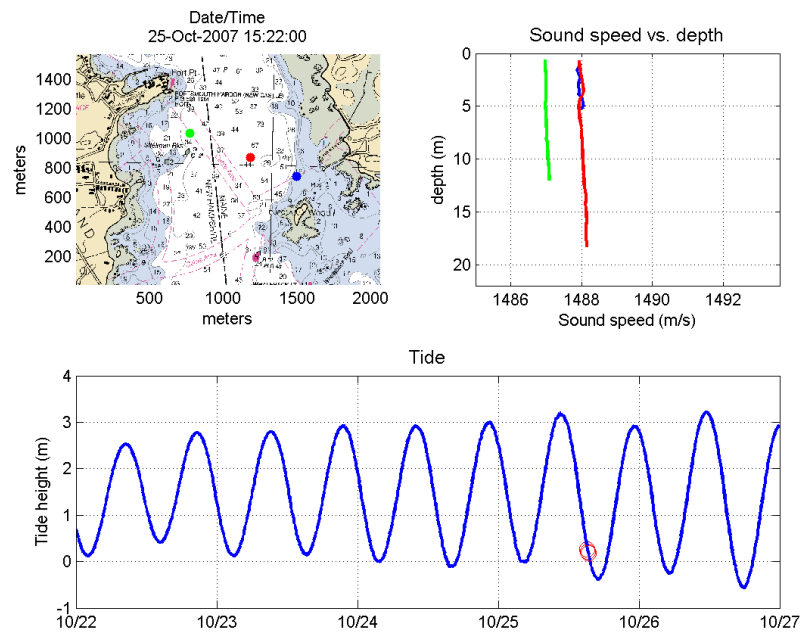Figure B-10: Sound speed transect 25 October 2007 at 14:32.

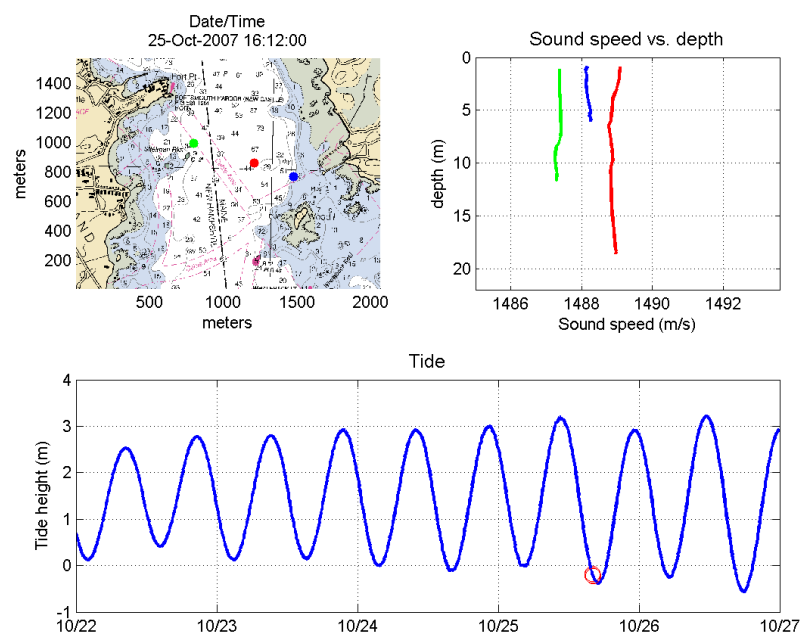Figure B-11: Sound speed transect 25 October 2007 at 15:22.

Figure B-12: Sound speed transect 25 October 2007 at 16:12.

APPENDIX C

Simple Geometry Model Results

The simple geometry model described in Section 3.2.1 was run for different source and receiver geometries. These results are shown below in Figures C-1 - C-5.
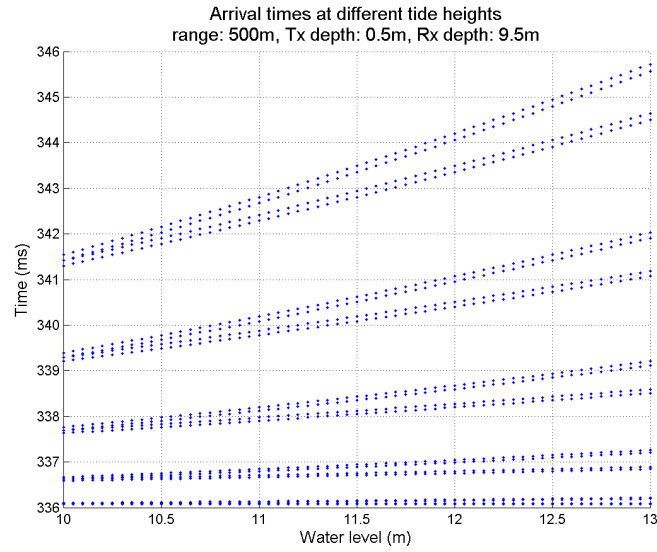

Figure C-1: Simple geometric model results for arrival time spacing using a source depth of 9.5 meters, a receiver depth of 0.5 meters, and a range of 500 meters.

Figure C-2: Simple geometric model results for arrival time spacing using a source depth of 9.5 meters, a receiver depth of 0.5 meters, and a range of 250 meters.

Figure C-3: Simple geometric model results for arrival time spacing using a source depth of 5 meters, a receiver depth of 5 meters, and a range of 950 meters.

Figure C-4: Simple geometric model results for arrival time spacing using a source depth of 0.5 meters, a receiver depth of 0.5 meters, and a range of 950 meters.
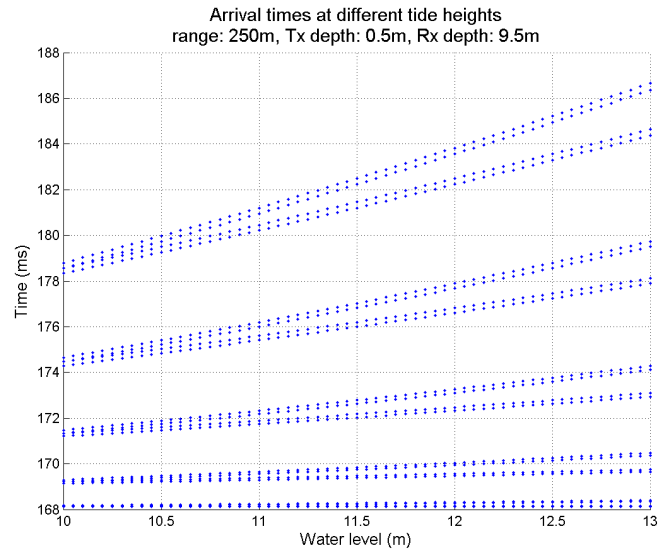

Figure C-5: Simple geometric model results for arrival time spacing using a source depth of 9.5 meters, a receiver depth of 9.5 meters, and a range of 950 meters.
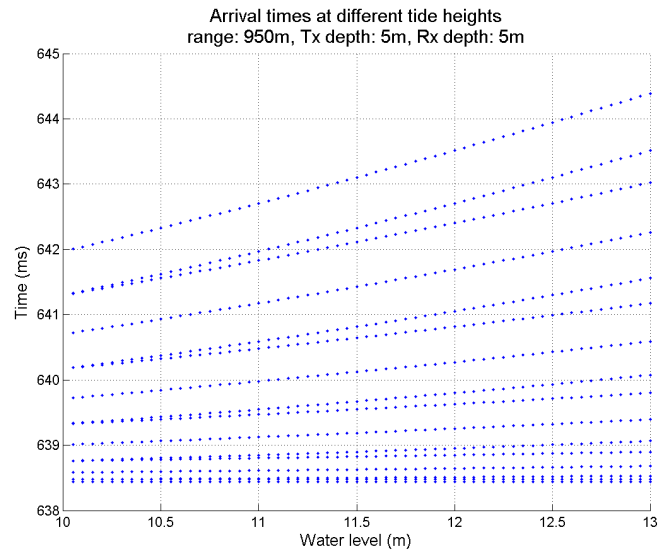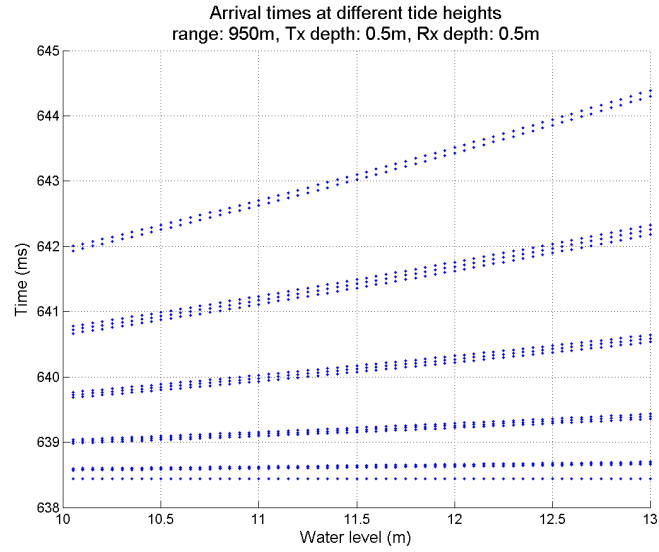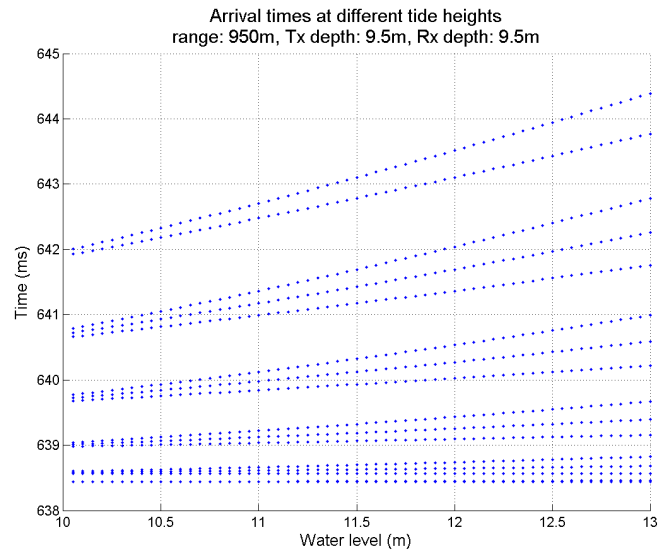
APPENDIX D

Ray Tracing Results for Different Source and Receiver Heights

Figure D-1 shows the ray paths for a source and receiver that are both close to the surface, in a completely isovelocity water column. A direct path arrival is visible between the two.

Figure D-1: Ray trace results for a source and receiver both located at a depth of 0.3 meters, with a constant sound speed throughout the water column.

Figure D-2 shows the ray paths that would result from the source and receiver near the surface, and a sound speed profile with a linear gradient. This extreme downward refracting

environment would prevent direct path arrivals but would allow one-bounce arrivals.
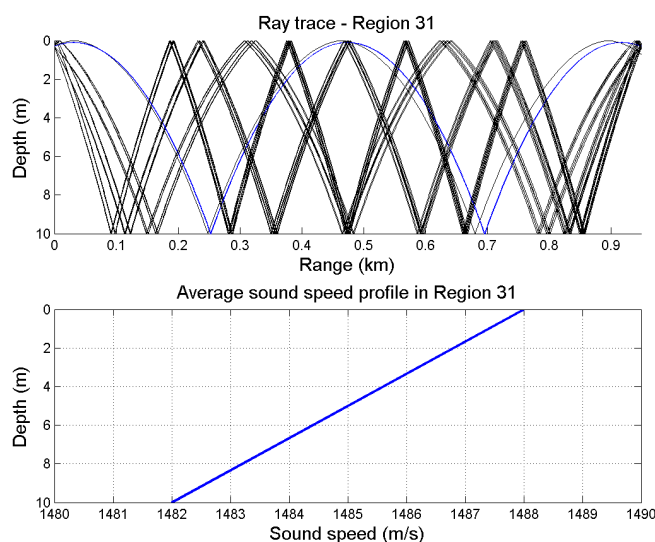
Figure D-2: Ray trace results for a source and receiver both located at a depth of 0.3 meters, with a linear sound speed profile (8 m/s change over a depth of 10 meters).

The ray tracing arrival times that would result from gradually increasing linear sound speed gradients are shown in Figure D-3.

If the source and receiver are both very close to the bottom, a different structure occurs. Ray tracing results for the isovelocity case when the source and receiver are near the bottom are shown in Figure D-4.

The ray tracing results for a source and receiver near the bottom with a higher gradient sound speed structure are shown in Figure D-5.

The ray tracing arrival times that would result from gradually increasing linear sound speed gradients are shown in Figure D-6.

These ray tracing results indicate that the arrival group geometry is very sensitive to the source receiver geometry. Additional care should be taken when sources and receivers are very close to the boundaries, particularly considering the strong downward refracting

Figure D-3: Arrival times predicted by ray tracing using linear sound speed profiles (source and receiver near the surface).
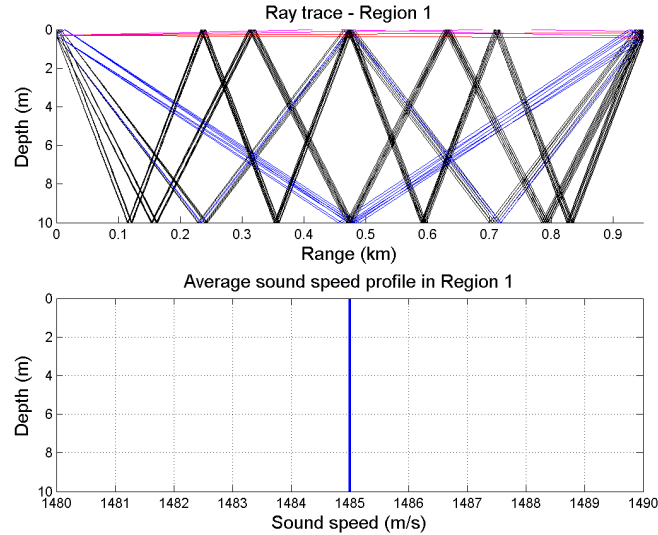
sound speed profiles that have been measured.

Figure D-4: Ray trace results for a source and receiver both located at a depth of 9.7 meters, with a constant sound speed throughout the water column.

Figure D-5: Ray trace results for a source and receiver both located at a depth of 9.7 meters, with a linear sound speed profile (8 m/s change over a depth of 10 meters).
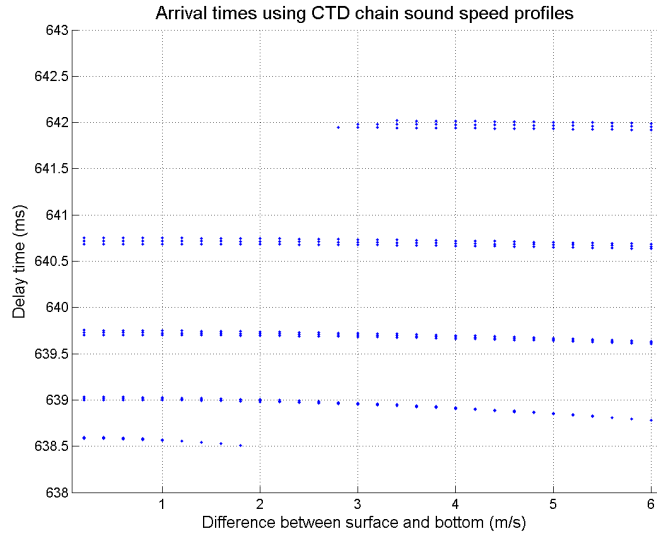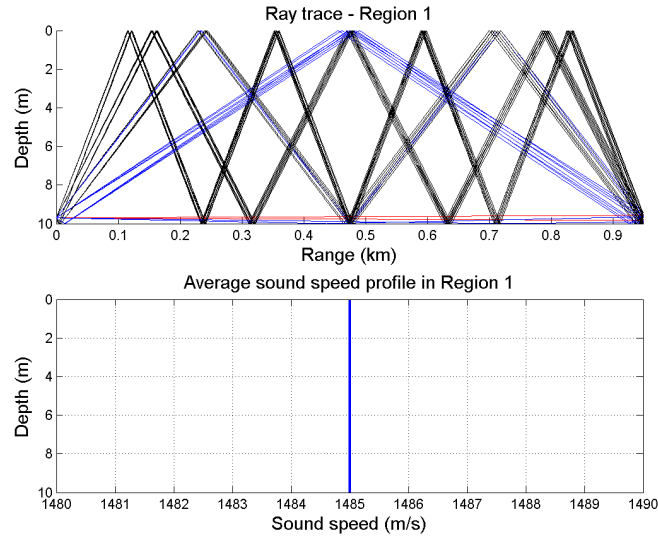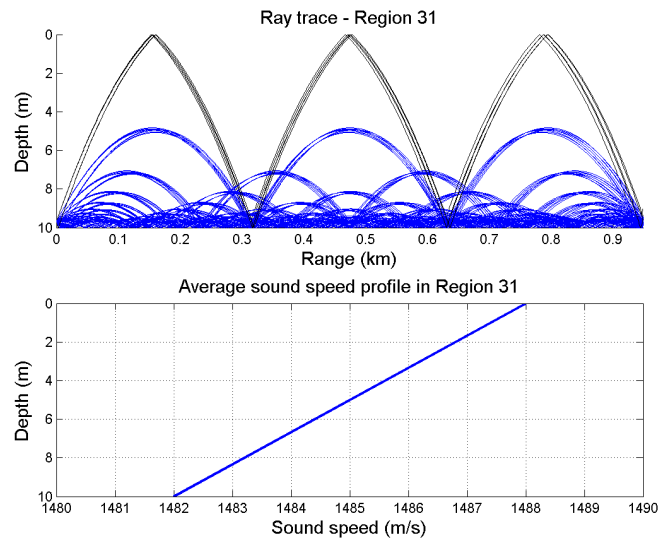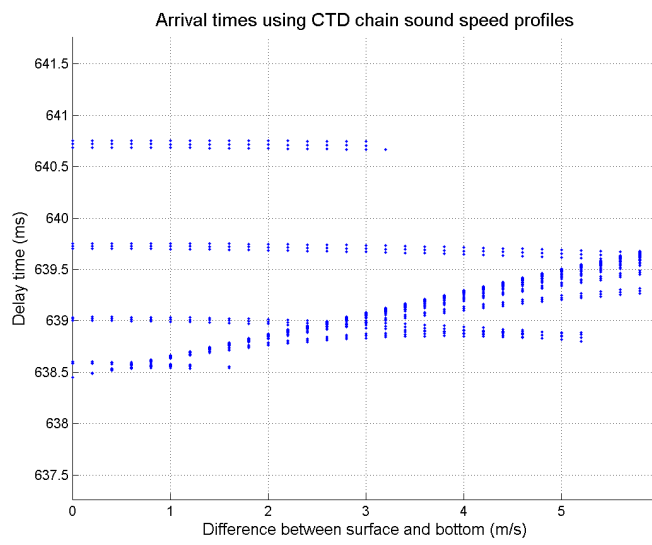
Figure D-6: Arrival times predicted by ray tracing using linear sound speed profiles (source and receiver near the bottom).

BIBLIOGRAPHY

[1] L. Ward, "Sedimentology of the Lower Great Bay / Piscataqua River Estuary," Department of the Navy, NCCOSC RDTE Division, Tech. Rep., 1995.

[2] B. J. Kraft, L. Fonseca, L. Mayer, G. McGillicuddy, J. Ressler, J. Henderson, and P. G. Simpkin, "In situ measurements of sediment acoustic properties and relationship to multibeam backscatter," *The Journal of the Acoustical Society of America*, vol. 115, no. 5, pp. 2401–2402, May 2004.

[3] C. Gostnell, "Efficacy of an interferometric sonar for hydrographic surveying: Do interferometers warrant an in depth examination?" *The Hydrographic Journal*, no. 118, pp. 17–24, October 2005.

[4] S. Pe'eri, L. Morgan, W. Philpot, and G. Guenther, "Lidar as a shorline mapping tool," in *Proceedings of the U.S. Hydrographic Conference*, Norfolk, VA, May 2007.

[5] Y. Rzhanov, L. Huff, and R. G. Cutter, "Seafloor video mapping: modeling, algorithms, apparatus." in *ICIP (1)*, 2002, pp. 868–871.

[6] J. J. Leonard, A. A. Bennet, C. M. Smith, and H. J. S. Feder, "Autonomous underwater vehicle navigation," Massachussetts Institute of Technology, MIT Marine Robotics Laboratory, Cambridge, MA, Tech. Rep., 1998.

[7] L. Whitcomb, D. Yoerger, and H. Singh, "Advances in doppler-based navigation of underwater robotic vehicles," in *IEEE International Conference on Robotics and Automation*, vol. 1, May 1999, pp. 399–406.

[8] D. Titterton and J. Weston, *Strapdown Inertial Navigation Techniques*, ser. 5. Stevenage, United Kingdom: Peter Perigrinus Ltd., 1997.

[9] P. Milne, *Underwater Acoustic Positioning Systems.* Houston, TX: Gulf Publishing Company, 1983.

[10] D. Phillip, "An evaluation of USBL and SBL acoustic systems and the optimisation of methods of calibration - part 1," *The Hydrographic Journal*, no. 108, pp. 18–25, April 2003.

[11] K. Vickery, "Acoustic positioning systems - a practical overview of current systems," in *Proceedings of IEEE Workshop on Autonomous Underwater Vehicles.* IEEE, 1998a, pp. 5–17.

[12] ——, "Acoustic positioning systems, new concepts - the future," in *Proceedings of the 1998 Workshop on Autonomous Underwater Vehicles.* IEEE, 1998b, pp. 103–110.

[13] A. Alcocer, P. Oliveira, and A. Pascoal, "Underwater acoustic positioning systems based on buoys with GPS," in *Proceedings of the Eighth European Conference on Underwater Vehicles*, S. Jesus and O. Rodriguez, Eds., Carvoeiro, Portugal, June 2006.

[14] P. Milne, *Underwater Engineering Surveys.* Houston, TX: Gulf Publishing Company, 1980.

[15] M. Deffenbaugh, J. G. Bellingham, and H. Schmidt, "The relationship between spherical and hyperbolic positioning," in *MTS/IEEE Oceans Conference Proceedings - 'Prospects for the 21st Century'*, vol. 2. IEEE, September 1996, pp. 590–595.

[16] M. Wikström, U. Ahnström, J. Falk, and P. Händel, "Implementation of an acoustic location-finding system for TDOA measurements," in *Nordic Matlab Conference 2003*, October 2003.

[17] J. P.W. Smith, "The avered impulse response of a shallow-water channel," *The Journal of the Acoustical Society of America*, vol. 50, no. 1, pp. 332–336, January 1971.

[18] R. Aubauer, M. O. Lammers, and W. W. L. Au, "One-hydrophone method of estimating distance and depth of phonating dolphins in shallow water," *The Journal of the Acoustical Society of America*, vol. 107, no. 5, p. 2744, 2749 2000.

[19] M. Deffenbaugh, H. Schmidt, and J. G. Bellingham, "Acoustic positioning in a fading multipath environment," in *IEEE Oceans Conference*, Ft. Lauderdale, Florida, September 1996, pp. 596–599.

[20] R. J. Urick, *Principles of Underwater Sound*, 3rd ed. Los Altos, CA: Peninsula Publishing, 1983.

[21] D. Di Iorio and D. M. Farmer, "Separation of current and sound speed in the effective refractive index for a turbulent environment using reciprocal acoustic transmission," *The Journal of the Acoustical Society of America*, vol. 103, no. 1, pp. 321–329, January 1998.

[22] R. W. Meredith, S. J. Stanic, R. R. Goodman, E. T. Kennedy, and N. G. Pace, "Comparisons of high-frequency acoustic fluctuations with ocean temperature and sea-surface fluctuations in shallow water," *IEEE Journal of Oceanic Engineering*, vol. 29, no. 2, pp. 524–533, April 2004.

[23] K. Mackenzie, "Long-range shallow-water signal-level flucutations and frequency spreading," *The Journal of the Acoustical Society of America*, vol. 34, no. 1, pp. 67–75, January 1962.

[24] P. H. Dahl, "On bistatic sea surface scattering: Field measurements and modeling," *The Journal of the Acoustical Society of America*, vol. 105, no. 4, pp. 2155–2169, April 1999.

[25] S. T. McDaniel, "Sea surface reverberation: A review," *The Journal of the Acoustical Society of America*, vol. 94, no. 4, pp. 1905–1922, October 1993.

[26] J. W. Choi and P. H. Dahl, "Mid-to-high-frequency bottom loss in the East China Sea," *IEEE Journal of Oceanic Engineering*, vol. 29, no. 4, pp. 980–987, October 2004.

[27] D. Rouseff and T. E. Ewart, "Effect of random sea surface and bottom roughness on propagation in shallow water," *The Journal of the Acoustical Society of America*, vol. 98, no. 6, pp. 3397–3404, December 1995.

[28] W. Stone, "The evolution of the National Geodetic Survey's continuously operating reference station network and online positioning user service," ION-IEEE Position, Location, and Navigation Symposium, San Diego, CA, August 2008.

[29] J. M. Anderson and E. M. Mikhail, *Surveying: Theory and Practice*, 7th ed. Boston, MA: WCB/McGraw-Hill, 1998.

[30] G. Seeber, *Satellite Geodesy*, 2nd ed. Berlin, Germany: Walter de Gruyter, 2003.

[31] M. Cooper, *Control Surveys in Civil Engineering*. London, Great Britain: Nichols Publishing Company, 1987.

[32] W. S. Burdic, *Underwater Acoustic System Analysis*, 2nd ed. Englewood Cliffs, NJ: Prentice-Hall, 1991.

[33] J. Schneibel, E. George, I. Anderson, and J. Sellschopp, "A towed CTD chain for two-dimensional high resolution hydrography," *Deep Sea Research Part I: Oceanographic Research Papers*, vol. 44, no. 1, pp. 147–165, January 1997.

[34] V. del Grosso, "New equation for the speed of sound in natural waters with comparisons to other equations," *The Journal of the Acoustical Society of America*, vol. 56, no. 4, pp. 1084–1091, October 1974.

[35] R. Pawlowicz, B. Beardsley, and S. Lentz, "Classical tidal harmonic analysis including error estimates in matlab using t_tide," *Computer and Geosciences*, vol. 28, no. 8, pp. 929–937, October 2002.

[36] E. L. Hamilton, "Geoacoustic modeling of the sea floor," *The Journal of the Acoustical Society of America*, vol. 68, no. 5, pp. 1313–1340, November 1980.

[37] M. B. Porter and H. P. Bucker, "Gaussian beam tracing for computing ocean acoustic fields," *The Journal of the Acoustical Society of America*, vol. 82, no. 4, pp. 1349–1359, October 1987.

[38] D. Di Iorio and D. M. Farmer, "Path-averaged turbulent dissipation measurements using high-frequency acoustical scintillation analysis," *The Journal of the Acoustical Society of America*, vol. 96, no. 2, pp. 1056–1069, August 1994.

[39] H. Tennekes and J. Lumley, *A First Course in Turbulence.* Cambridge, MA: The MIT Press, 2001.

[40] C. S. Clay and H. Medwin, *Acoustical Oceanography: Principles and Applications.* New York, NY: Wiley-Interscience, 1977.

[41] B. Cotté, R. L. Culver, and D. L. Bradley, "Scintillation index of high frequency acoustic signals forward scattered by the ocean surface," *The Journal of the Acoustical Society of America*, vol. 121, no. 1, pp. 120–131, April 2007.

[42] C. D. Ghilani and P. R. Wolf, *Adjustment Computations - Spatial Data Analysis.* Hoboken, NJ: John Wiley and Sons, Inc., 2006.

[43] A. L. Allan, *Maths for Mapmakers*, 2nd ed. Caithness, Scotland: Whittles Publishing, 2004.

[44] E. M. Mikhail and G. Gracie, *Analysis and Adjustment of Survey Measurements.* New York, NY: Van Nostrand Reinhold Company, 1981.